

This work was written as part of one of the author's official duties as an Employee of the United States Government and is therefore a work of the United States Government. In accordance with 17 U.S.C. 105, no copyright protection is available for such works under U.S. Law. Access to this work was provided by the University of Maryland, Baltimore County (UMBC) ScholarWorks@UMBC digital repository on the Maryland Shared Open Access (MD-SOAR) platform.

Please provide feedback

Please support the ScholarWorks@UMBC repository by emailing scholarworks-group@umbc.edu and telling us what having access to this work means to you and why it's important to you. Thank you.

Recreating the Horizontal Magnetic Field at Colaba during the Carrington Event with Geospace Simulations

Seán P. Blake^{1,2}, Antti Pulkkinen², Peter W. Schuck², Alex Gloer², Denny

M. Oliveira^{3,2}, Daniel Welling⁴, Robert S. Weigel⁵, Gary Quaresima⁵

The ‘Carrington event’ geomagnetic storm was simulated with an extremely impulsive solar wind and the SWMF.

This simulation was able to reproduce the low-latitude B_H signal measured at Colaba during the Carrington event.

A combination of magnetopause adjacent currents and low-latitude FACs were responsible for the negative B_H at the dayside.

Corresponding author: Seán P. Blake, NASA Goddard Space Flight Center, Heliophysics Science Division, USA (sean.blake@nasa.gov)

¹Department of Physics, Catholic

D R A F T

February 27, 2021, 6:04pm

D R A F T

This article has been accepted for publication and undergone full peer review but has not been through the copyediting, typesetting, pagination and proofreading process, which may lead to differences between this version and the [Version of Record](#). Please cite this article as [doi: 10.1029/2020SW002585](#).

This article is protected by copyright. All rights reserved.

Abstract.

An intriguing aspect of the famous 2 September 1859 geomagnetic disturbance (or ‘Carrington’ event) is the horizontal magnetic (B_H) dataset measured in Colaba, India (magnetic latitude approximately 20 degrees N). The field exhibits a sharp decrease of over 1600 nT and a quick recovery of about 1300 nT, all within a few hours during the daytime. The mechanism behind this has previously been attributed to magnetospheric processes, ionospheric processes or a combination of both. In this paper, we outline our efforts to replicate this low-latitude magnetic field using the Space Weather Modelling

University of America, Washington, District
of Columbia, USA

²NASA Goddard Space Flight Center,
Heliophysics Science Division, Greenbelt,
Maryland, USA

³Goddard Planetary Heliophysics
Institute, University of Maryland, Baltimore
County, Baltimore, Maryland, USA

⁴University of Texas at Arlington Physics
Department, Arlington, TX, USA

⁵Physics and Astronomy Department,
George Mason University, Fairfax VA, USA

19 Framework (SWMF). By simulating an extremely high pressure solar wind
20 scenario, we can emulate the low-latitude surface magnetic signal at Colaba.
21 In our simulation, magnetospheric currents adjacent to the near-Earth mag-
22 netopause and strong Region 1 field-aligned currents (FACs) are the main
23 contributors to the large Colaba B_H . The rapid recovery of B_H in our sim-
24 ulated scenario is due to the retreat of these magnetospheric currents as the
25 magnetosphere expands, as opposed to ring current dynamics. In addition,
26 we find that the scenario that best emulated the surface magnetic field ob-
27 servations during the Carrington event had a minimum calculated Dst value
28 between -431 and -1191 nT, indicating that Dst may not be a suitable es-
29 timate of storm intensity for this kind of event.

1. Introduction

The Carrington event of 1-2 September 1859 is one of the largest geomagnetic storms on record and has been extensively studied as an example of a geomagnetic superstorm. It was preceded by the first observation of a solar flare on 1 September 1859 and had widespread effects across the globe including extremely low-latitude visible overhead aurora (seen as far equatorward as locations such as Cuba and the South of Japan) [Shea & Smart, 2006; Hayakawa *et al.*, 2019; Kimball, 1960; Green & Boardsen, 2006; González-Esparza & Cuevas-Cardona, 2018], widespread geomagnetic disturbances [Blake *et al.*, 2020; Cliver & Dietrich, 2013], and significant disruption to telegraph operations [Boteler, 2006; Clark, 2007]. It is likely to have been more intense than any geomagnetic storm that has occurred in the satellite era, and there have been many efforts to classify its intensity in terms of Dst, a proxy measurement for the strength of the ring current, and a commonly used measure of storm intensity since 1957 [Tsurutani *et al.*, 2003; Siscoe *et al.*, 2006; Cliver & Dietrich, 2013]. These various estimations, which were arrived at by both analysis of limited observations and modelling, range from around -600 nT to -1160 nT [Cliver & Dietrich, 2013]. For context, the largest geomagnetic storm for which the Dst has been definitively measured was the 13-14 March 1989 event with minimum $Dst = -589$ nT. The effects of the 1989 geomagnetic storm were intense enough to disrupt the Hydro-Quebec power system [Allen *et al.*, 1989; Bolduc, 2002; Boteler, 2019], and were a Carrington-scale geomagnetic storm to occur today, it would probably result in widespread negative effects in grounded infrastructure such as long-distance power transmission grids [Oughton *et al.*, 2017; Pulkkinen *et al.*, 2017].

The Carrington event occurred when numerous geomagnetic observatories were already operational around the world. By 1859, geomagnetic observatories were operating in locations such as Russia, Canada, Australia, Britain, Italy, and Norway (among others) [Nevanlinna & Häkkinen, 2010; Shea & Smart, 2006; Aplin & Harrison, 2014; Blake et al., 2020]. Despite the numerous measurements taken at that time, the equipment used to measure the intensity and direction of Earth's surface geomagnetic field had its limitations [Blake et al., 2020]. One such limitation was that measurements often needed to be taken manually, leading to long gaps between measurements [Curto, 2020]. The manpower needed for high-frequency measurements to be taken continuously was often not available at these early observatories. This can be seen in the Madras observatory for example, which took horizontal measurements once per hour, except on Sundays when no measurements were taken [Jacob, 1884]. For large geomagnetic storms in particular, even hourly measurements could lead to rapid geomagnetic variations being missed [Viljanen et al., 2014]. Even where this was not a problem (such as with the continuously recording magnetograms used in British observatories [Boteler, 2006]), the devices often went beyond their operational range during geomagnetic disturbances. For example, the horizontal magnetometer operated in Rome during the Carrington event had an operational range of only around 300 nT [Blake et al., 2020]. This lack of complete and useful measurement sets makes it difficult to study the evolution of the geomagnetic field during the Carrington event.

Presently, the most important set of horizontal magnetic field measurements that exists for the Carrington event is from Colaba (near modern-day Mumbai, 18.9° N, 72.8° E) [Tsurutani et al., 2003; Kumar et al., 2015]. Unlike other datasets, these measurements

were taken with a relatively high cadence (beginning with one measurement every hour, increasing to once every 5 minutes as the geomagnetic field became more disturbed), and does not appear to go off-scale at any point. This horizontal magnetic field (B_H) dataset is seen to decrease by $\sim 1,600$ nT over two hours, then rapidly increase by $\sim 1,250$ nT over 20 minutes. The rapidity and magnitude of the magnetic deflection and recovery is unique among low-latitude B_H measurements in the records. The mechanism which explains this signal is uncertain, and different hypotheses have been suggested in the literature. The simultaneity of disturbances at different latitudes on the morning of 02 September 1859 has led some to suggest that the signal is at least partly due to the encroachment of currents from the ionosphere [Green & Boardsen, 2006; Cliver & Dietrich, 2013]. Siscoe et al. [2006] interpreted the Colaba B_H time-series as having been produced by magnetospheric instead of ionospheric currents. Keika et al. [2015] suggests that the rapid recovery is due to the relaxation of the equatorial ring current due to the flow-out of energetic ions. Cid et al. [2015] suggests that field-aligned currents (FACs) played a major role in the magnitude of B_H .

Colaba is a low-latitude location and so the B_H measurements taken there are often used to characterise the Carrington event in terms of Dst [Li et al., 2006; Siscoe et al., 2006; Keika et al., 2015], which is normally calculated from four low-latitude observatory measurements [Love & Gannon, 2009]. Dst for the 2 September 1859 has been estimated using the Colaba dataset as a spot-measurement [Tsurutani et al., 2003] or an hourly average [Siscoe et al., 2006; Gonzalez et al., 2011]. Using these Dst estimates, the solar wind conditions that gave rise to the geomagnetic storm can then be estimated using

empirical relations such as the Burton equation [*Burton et al.*, 1975], or its modified version [*O'Brien & McPherron*, 2000].

Studies that attempt to reproduce the large decrease and rapid recovery in Dst using these models often used very high speed ($> 2,000 \text{ km s}^{-1}$), very negatively B_Z ($< -80 \text{ nT}$) and high density solar wind. For example, *Li et al.* [2006] required an extremely high solar wind density of almost $2,000 \text{ particles cm}^{-3}$. By extending the Burton model to include ion flow-out, *Keika et al.* [2015] were able to reproduce a Dst of $\sim -1,600 \text{ nT}$ and a rapid recovery using a solar wind density of $100 \text{ particles cm}^{-3}$.

In addition to the analyses outlined above, large-scale magnetospheric simulations have also been used to numerically simulate extreme events up to and beyond estimated Carrington-scale storms [*Ngwira et al.*, 2013, 2014; *Welling et al.*, 2020; *Blake et al.*, 2020b]. These magnetohydrodynamic (MHD) models include the Lyon-Fredder-Mobarry (LFM) model [*Lyon et al.*, 2004], the Grand Unified Magnetosphere-Ionosphere Coupling Simulation (GUMICS) [*Janhunen et al.*, 2012] and the Block-Adaptive-Tree-Solarwind-Roe-Upwind-Scheme (BATS-R-US) model [*Powell et al.*, 1999; *De Zeeuw et al.*, 2000]. Each of these can be used to study different phenomena that occur during geomagnetic storms [*Welling*, 2019].

In this paper, we use the BATS-R-US as part of the Space Weather Modeling Framework (SWMF) to simulate the Carrington event, with particular focus on reproducing the intense dip and recovery at Colaba. As inputs for this storm simulation, we used solar wind conditions that resulted in an extremely high solar wind pressure exerted on the magnetosphere. These solar wind conditions were scaled to extreme but not unreasonable values for speed, and density. We find that as the simulated magnetopause is compressed,

currents adjacent to the magnetopause are the likely cause of an extreme decrease in the dayside surface magnetic field at low latitudes. As the solar wind pressure decreases, these currents retreat, allowing the rapid recovery of the low-latitude surface magnetic field. Finally, we calculate the Dst for our simulated storm event. We find that due to the unusual nature of the simulated event, Dst may not be a suitable measure for its intensity.

2. Simulation Setup

For this study, we use the SWMF to simulate our Carrington-scale storm event. The SWMF is a software framework for physics-based simulations of the Sun-Earth system [Toth *et al.*, 2005, 2012]. It allows for different physics models to be combined in order to simulate across a large range of spatial scales, from the solar corona to the Earth's upper atmosphere and ionosphere. Our study uses solar wind conditions at L1 as inputs, and simulates the magnetosphere and ionosphere, as well as the FACs which connect them. The model used in this study consists of the Block Adaptive Tree Solar wind Roe-type Upwind Scheme (BATS-R-US) coupled to the Rice Convection Model for the inner magnetosphere (RCM), as well as the Ridley Ionosphere Model (RIM).

BATS-R-US is an MHD model that calculates the plasma conditions in the general magnetosphere domain of the simulation and uses a block-adaptive mesh grid. Blocks of higher resolution cells can be specified for regions of interest such as near-Earth locations or the magnetotail [Powell *et al.*, 1999; De Zeeuw *et al.*, 2000]. RCM captures ring current dynamics by receiving magnetic field values and plasma moments from BATS-R-US, and returns plasma density and pressure back to BATS-R-US [Toffoletto *et al.*, 2003; De Zeeuw *et al.*, 2004]. RIM is a height-integrated ionospheric electrodynamics model, which calculates the currents on a 2D ionospheric shell [Ridley *et al.*, 2004]. It receives field-

aligned current density from BATS-R-US and communicates electric potential to RCM and BATS-R-US. The communication between each of these separate models is facilitated by the SWMF, and is heavily dependent on the ionospheric conductance [Ngwira *et al.*, 2014]. This conductance is due to solar EUV ionization (a function of solar zenith angle) and particle precipitation. This latter component is dependent on FACs in RIM, with the relation between FACs and conductance having been derived from empirical data [Welling, 2019]. For our simulation, the nightside and polar cap Pedersen conductances were assumed to be 1 and 0.25 mho respectively.

This combination of BATS-R-US, RIM and RCM is widely used for geomagnetic storm simulations. It has been shown to perform well when statistically replicating surface dB/dt [Pulkkinen *et al.*, 2013] and Dst [Haiducek *et al.*, 2017], and has been used to study extreme geomagnetic storm events [Ngwira *et al.*, 2013, 2014; Welling *et al.*, 2020; Blake *et al.*, 2020b]. In order to calculate the surface geomagnetic field variations during the simulation, the Biot-Savart law is applied to the currents in each of the simulated domains: the magnetosphere, the ionosphere (Hall and Pedersen) and the gap-region FACs which connect them [Yu & Ridley, 2008; Yu *et al.*, 2010]. The total magnetic field variation at a point on the Earth's surface is equal to the sum of these contributions. As the 1859 Colaba dataset was sampled at best at 5 min, the surface magnetic field for our simulation was calculated on a $1^\circ \times 1^\circ$ geographic grid every 60s.

The magnetospheric grid used for this simulation had approximately 5.89 million cells, which ranged in size from $8 R_E$ in the far tail to $1/16 R_E$ near the Earth. The grid used for this simulation is shown in Figure 1. The inner magnetosphere boundary of the simulation was set at $1.5 R_E$ and the magnetopause currents were mapped from a

radius of $1.8 R_E$ to the ionosphere along assumed dipole lines. The coupling time between the different modules was set to 2 s, in order to capture the rapidly varying ionospheric currents under the extreme solar wind driving conditions. The grid resolution for RIM was 2° in longitude and 1° in latitude.

By default, the Earth's rotational axis is determined by the date and time given by the time of the simulation. In order to better recreate the conditions of the Carrington event, three additional steps were taken in the setup of the simulation. The dipole strength of the Earth in the SWMF simulation was changed to 32,000 nT. This is the approximate value given by the GUFM1 model for 1859 [Jackson *et al.*, 2000]. In addition, the position of the magnetic axis at the start of the run was set such that the magnetic North pole was at 69.174° N, 96.757° W, its approximate position in 1859 (calculated using the GUFM model, www.ngdc.noaa.gov/geomag/GeomagneticPoles.shtml). This corresponds to colatitude Θ and longitude Φ angles of 16.52° and -130.32° in GSE coordinates. Finally, the solar radio flux $F_{10.7}$ (which affects ionospheric conductance) was set to 192 solar flux units. The solar $F_{10.7}$ flux is highly correlated to sunspot number [Okoh & Okoro, 2020], and the monthly mean sunspot for September 1859 of 200, taken from www.sidc.be/silso was used to estimate this $F_{10.7}$ value.

2.1. Solar Wind Conditions

For this study, we created two synthetic solar wind scenarios to use as inputs for our simulated Carrington events. The measured horizontal magnetic field time-series taken at Colaba was used as a template for the shape of each of the solar wind components:

magnetic field, velocity, particle density and temperature. Our general aim for the solar wind inputs was to produce an extremely fast solar wind with a high ram pressure, which would highly compress the magnetopause. To achieve this, each of the solar wind components were scaled to particular values so that they peaked at $\sim 06:30$ GMT, when the Colaba B_H was at its most disturbed condition. The first solar wind scenario ('Scenario 1') gradually reduces in intensity after 06:30 GMT, following the Colaba B_H time-series. The second solar wind scenario ('Scenario 2') immediately reverts to quiet solar wind conditions after 06:30 GMT. Finally, Scenario 1 was run again without the RCM component ('Scenario 3'). These contrasting scenarios were simulated in order to better quantify the effect of the ring current, as shall be shown in Section 3. Figure 2 shows the measured B_H at Colaba in 1859 (top panel), and each of the solar wind conditions for the two scenarios (bottom panels).

For simplicity, the V_Y and V_Z components of the solar wind were set to zero. The incoming solar wind structure was therefore purely frontal, which maximizes the effects of its symmetric impact [Oliveira & Samsonov, 2018; Rudd *et al.*, 2019]. The V_X (Earthward) component of the solar wind peaks at $2,500 \text{ km s}^{-1}$. This represents an extremely fast Earthward velocity for a CME at 1 AU. This is slightly slower than the extreme scenario of $\sim 2,700 \text{ km s}^{-1}$ outlined in Tsurutani & Lakhina [2014] (and simulated in Welling *et al.* [2020]). Tsurutani & Lakhina [2014] suggests that for such a high speed CME, interplanetary space would likely need to be 'cleaned out' by a previous CME, in order to reduce drag. Manchester *et al.* [2005] simulated a single very fast CME that travelled to Earth in 18 h (equivalent to the estimated 17 h 40 m for the Carrington event). In order to achieve this, they needed an initial speed of $4,000 \text{ km s}^{-1}$ at the Sun. The speed reduced

to $\sim 2,000 \text{ km s}^{-1}$ by the time the CME had reached 1 AU. Such extreme speeds have been measured in solar wind at 1 AU. In-situ measurements of the July 2012 CME taken by NASA's STEREO-A spacecraft recorded a speed of approximately $2,500 \text{ km s}^{-1}$ [Ngwira *et al.*, 2013], and the August 1972 event had an average speed of around $2,850 \text{ km s}^{-1}$ [Hoffman *et al.*, 1975; Zastenker, 1978].

The solar wind density is set to around 25 cm^{-3} at the start of the simulation. It then begins to gradually increase at 04:50. Following this, the density increases rapidly to a peak of 95 cm^{-3} at 06:30 GMT. This peak, coinciding with the time of maximum Earthward velocity, results in a maximum solar wind pressure of $\sim 1,000 \text{ nPa}$ at 06:30 GMT. While this peak density is large, similar values have been measured in the solar wind before [Tsurutani *et al.*, 2017].

For simplicity again, the solar wind B_X and B_Y components were also set to zero. A maximum intensity for the magnetic field of the solar wind inputs was set at 118 nT. This value is calculated from the empirical relationship between velocity and B_z of magnetic clouds at 1 AU recorded by Gonzalez *et al.* [1998]:

$$B_{peak}(\text{nT}) = 0.047 V_{peak}(\text{kms}^{-1}) \quad (1)$$

Although we note here that this relationship is derived from a limited dataset with peak B intensities of $< 40 \text{ nT}$. With our maximum V_X equal to $2,500 \text{ km s}^{-1}$, and our B_X , B_Y set to 0, this gives a minimum B_Z equal to -118 nT . This is slightly smaller in amplitude than the 'perfect' CME scenario given by Tsurutani & Lakhina [2014] (which had a $B_Z = -127 \text{ nT}$). Lastly, the temperature was scaled to a maximum of approximately 6 MK. This is similar to the maximum temperature of the July 2012 fast CME. Once all

of the solar wind components were constructed, small levels of noise drawn from normal distributions with standard deviation proportional to the amplitude of each of the solar wind components were added, in order to mimic the small scale fluctuations in the solar wind.

3. Simulation Results

The simulations were each run for approximately 12 hours (from 04:10 GMT to 16:00 GMT). The top rows in Figure 3 show the normalized total current density (J) in the near-Earth GSE XZ -plane (top) and the pressure in the $X - Y$ plane (middle) for three different times during the Scenario 1 simulation. These times correspond to pre-storm (column A), when the magnetopause was at its most compressed (column B) and during the main phase of the storm (column C). The black and white lines are open and closed field lines in the XZ plane. The red lines are the closed field lines whose footprints are closest to the poles. The location of the magnetopause standoff distance is calculated from these lines. The third row shows the magnetopause standoff distance for Scenario 1 (red line) and Scenario 2 (blue line) for the duration of the simulations. The bottom row shows the SWMF-derived Dst for each storm scenario. Vertical dashed black lines correspond to the times shown in the top two rows.

At the start of the simulations, the magnetopause is situated at approximately $8 R_E$. The position of the magnetopause was forced to a minimum standoff distance of $2.26 R_E$ at 06:30 GMT for both Scenarios 1 and 2 by the solar wind. This corresponds to the time when the input solar wind pressure was at its highest (at $\sim 1,000$ nPa). This extremely close standoff position is well within the orbit of many satellites, and would expose them to the solar wind environment, causing damaging surface charging [Koons & Fennell, 2006].

In Scenario 1, the subsolar magnetopause is expanded to a position $>5 R_E$ by 07:05 GMT, and it remains in the range $5 - 7.5 R_E$ for the rest of the simulation. For Scenario 2, as the solar wind immediately reverts to pre-storm conditions, the magnetopause rapidly expands and returns to a position $> 10 R_E$ by 07:40 GMT. After this, the magnetopause slowly returns to around $8 R_E$. For both scenarios, the minimum Dst calculated by the SWMF is -989 nT. This Dst is discussed further in Section 4.3.

3.1. Simulated B_H at Colaba

As mentioned above, the surface magnetic field was calculated for every minute of the simulation on a $1^\circ \times 1^\circ$ geographic grid. The magnetic field at each point on this grid is the sum of magnetic contributions from

1. All of the currents in the magnetospheric domain of the simulation
2. FACs in the region between the magnetospheric and ionospheric domains
3. The ionospheric domain of the simulation (Hall and Pedersen currents)

Panels A, B and C of Figure 4 show the historical (green) and SWMF simulated (red) B_H at Colaba, for Scenarios 1, 2 and 3 respectively. For each of the storm scenarios, the simulated B_H at Colaba exhibit an extremely negative B_H dip of $-1,800$ nT between 05:30 GMT and 06:30 GMT as the input solar wind conditions ramp up in intensity. Between 06:30 GMT and 08:00 GMT, the B_H for Scenario 1 recovers around $1,300$ nT, where it remains disturbed for the remainder of the day. Excluding the amplitude and timing of the sudden storm commencement, the simulated B_H broadly follows the actual Colaba B_H , although it slightly underestimates the recovery after 06:30 GMT by approximately 275 nT. For Scenario 2, the solar wind drivers are immediately returned to pre-storm

conditions at 06:30 GMT. At this time, the B_H recovers 1,390 nT over 5 minutes. From 06:35 GMT onwards, there is a steady recovery of around 50 nT per hour.

The bottom panels of Figure 4 show the different contributions to the SWMF calculated B_H at Colaba for the three scenarios. These are from the magnetosphere (B_H^{MAG} , purple), Birkeland FACs (B_H^{FAC} , black) and ionosphere (B_H^{IONO} , blue). Also shown are the dynamic solar wind pressures (P_{SW} , dotted green). For Scenario 1, at the peak of the B_H depression (06:30 GMT), currents in the magnetosphere can be seen to contribute most to the B_H at Colaba, with about -1,050 nT. Next in importance are the FACs, contributing around 720 nT. In comparison, the contribution from the ionosphere is largely insignificant, contributing around 50 nT.

Figure 5 shows the global surface magnetic field and the contributions from each of the simulation domains at 06:30 GMT for Scenario 1, when the magnetopause was at its most compressed. Panels A, B, C and D show absolute horizontal magnetic field contributions (note: the color scales are different for each panel). Panels E and F show the Northward contribution from FACs and magnetosphere respectively. The colorbars for these plots were limited to ± 1000 nT to better highlight magnetic conditions at the dayside.

Colaba is marked with a yellow star in each panel, and the solar equator is marked with a white line. From Panel A, the largest geomagnetic disturbances are generally in the regions around the geomagnetic poles (North of Canada and Antarctica at around 90° E). In addition, the low-latitude region around noon (at $\sim 90^\circ$ E) sees smaller, although still significant geomagnetic disturbances. Although being too southerly to be affected by ionospheric currents (Panel B), Colaba is situated such that it sees significant negative

B_N field contributions from both the FACs (Panel E) and the magnetosphere (Panel F), with the magnetosphere contributing the most in the region just North of the equator.

These will each be discussed in more detail in the next sections.

3.2. FAC contribution to surface B

FACs are mapped along assumed dipole field lines between the magnetosphere and ionosphere domains of the SWMF simulation. From Panels D and E of Figure 4, the amplitude of the contribution from FACs to the B_H at Colaba follows the amplitude of the dynamic solar wind pressure acting upon the magnetosphere for both solar wind scenarios. As the solar wind pressure increases, more energy is transported from the magnetosphere to the ionosphere, resulting in magnetic field contributions to the surface magnetic field.

The top panels of Figure 6 show the ionospheric radial current density in the Northern and Southern hemispheres at 06:30 GMT for Scenario 1. These show the footprints of the FACs in the ionosphere. At this time, the Region 1 currents dominate, and can be seen to extend significantly equatorward on the dayside. Region 1 currents, which flow at higher latitudes than Region 2 currents, connect to the outer magnetosphere, and given the proximity of the extremely compressed magnetopause and the position of the last closed field lines at 06:30 GMT (Panel B in Figure 3), these FACs may connect directly to the magnetopause.

The middle and bottom panels of Figure 6 show the ionospheric Hall and Pedersen conductances for the same time. Both conductance distributions show complicated nightside structures, which are likely due to the Region 2 FACs distributions.

Panels C and E of Figure 5 shows the magnetic effect of FACs on the ground. Colaba is situated nearly equidistant between the two sets of Region 1 currents in each hemisphere. The two Region 1 current systems contribute a very negative component in terms of B_N (Panel E, Figure 5). The 720 nT signal at Colaba from the FACs at 06:30 GMT appears to be due to a combination of FACs whose ionospheric footprints are in both hemispheres North and South of Colaba.

3.3. Magnetosphere contributions to surface B

The extreme solar wind pressure exerted on the magnetosphere forces the magnetopause to within 8,700 km of the Earth's surface at 06:30 GMT in our simulation. At this time, it is nearly directly above Colaba, which lies at approximately noon. The magnetopause flows East around the Earth, and so this setup should result in a strong positive B_N at the Earth's surface. However, this is the opposite of what we observe (see Panel F in Figure 5).

Figure 7 shows two cross-sections of azimuthal current density in the near-earth magnetosphere at 06:30 GMT for Scenario 1. The left panel shows the $Y = 0 R_E$ XZ-plane, and the right panel shows the $Z = 0.4 R_E$ XY-plane. Red areas indicate current flowing East, and blue indicates currents flowing West. From both of these cross-sections, the magnetopause current is clearly visible. Due to the tilt of the magnetic dipole, the magnetopause current is not symmetric around the $Y = 0$ plane, but is elevated by approximately 15° from the solar equator.

Immediately adjacent to the compressed magnetopause are regions of Westward flowing current. This is true in the XZ-plane, and XY-plane. The current in these regions are

less intense than that of the magnetopause, however, they cover a larger volume than the magnetopause, and can be seen to extend closer to the Earth in the XZ-plane. Panel F in Figure 5 shows North-South component of the magnetic field from the magnetospheric domain. The large negative B_N region over Asia is not symmetric around the solar equator, but is instead shifted Northward by approximately 20 degrees. This corresponds to the position of the magnetopause, and the Westward flowing current systems adjacent to the magnetopause.

Next, we look at the role of the ring current on the magnetic field at the dayside of the Earth. For our standard SWMF setup (BATS-R-US with RCM and RIM), the contribution from the magnetosphere to the ground magnetic field perturbation includes the effect of the ring current. While the ring current contribution itself is not separable from the total magnetospheric contribution in the model, we can use plots of the near-Earth pressure and the contrast between Scenario 1 and Scenario 2 to infer its importance. In addition, we can contrast Scenario 1 to Scenario 3, which was run without the RCM. RCM solves for the bounce-averaged drift convection of ions and electrons in the closed field line region. As the magnetopause is heavily compressed on the dayside of the Earth in our scenarios, this reduces the volume where ring currents can be trapped. For this case, the higher energy portion of the ring current will drift further outward due to conserve the 3rd adiabatic invariant. In addition, particles drifting from night to day are more likely to be lost. These effects should cause the depletion of the ring current on the dayside however during the most compressed part of the storm, there is a partial ring current concentrated in the pre-midnight sector, which should mitigate this effect.

On the other hand, strong storms have been shown to result in deeper penetration of energetic particles to lower L shells due to the strong convection electric field at this time [Li *et al.*, 1993; Zhao & Li, 2013]. Any portion of the ring penetrating to very low L shell could still exist on the dayside and would be closer to Earth than normal. Figure 3 shows a ring current concentrated at low L compared to normal conditions.

Figure 3 shows the near-Earth pressure for three time-periods for Scenario 1. Up to 06:30, there is an intense build up of pressure at the nightside of the Earth. After this time, as the magnetopause rapidly retreats then remains beyond $7.5 R_E$, the pressure wraps westwardly around the Earth until it envelops the Earth by around 08:00. This is the ring current that remains energised throughout the rest of the simulation as the solar wind continues to deposit energy into the magnetosphere. Panel D of Figure 4 shows this sustained B_H contribution to Colaba from the magnetosphere hours after the massive dip and recovery.

In Scenario 2, the solar wind conditions immediately revert to solar-quiet conditions at 06:30 GMT, and the magnetopause rapidly expands (bottom row, Figure 3). This corresponds to a marked recovery in the the B_H^{MAG} at the dayside of the Earth (Panel D in Figure 4) for five minutes, after which there is a steady decline in the B_H^{MAG} for the rest of the simulation. In the version of the RCM used in our SWMF setup, there are only two loss mechanisms: advective loss (i.e., advection of particles through the outer boundary) and a simple time-constant-based loss term meant to reproduce basic Dst recovery dynamics [Pulkkinen *et al.*, 2013]. For Scenario 2, the decay in B_H^{MAG} after 06:35 GMT is due to this constant decay of the excited ring current. This shows how the simulated ring current relaxes without any further solar wind driving.

The rapid recovery of 560 nT in B_H^{MAG} for Scenario 2 between 06:30 GMT and 06:35 GMT is due to the expansion of the magnetopause, and the retreat of the previously identified westward current lobes adjacent to it. In Scenario 1, we see a similar recovery of around 500 nT between 06:30 GMT and 07:30, which corresponds to the slower expansion of the magnetopause (Figure 3).

Finally, we look at the B_H at Colaba for the Scenario 1 simulation without RCM (Scenario 3, further images and movies of this simulation are given in the supporting information). As could be expected, for this simulation there was no significant build-up of charged particles in the near-Earth magnetosphere, and no ring-current formation. Despite this, dip and recovery in B_H similar to Scenario 1 can still be seen at Colaba (panels C and F in Figure 4). In this case, the magnetospheric currents and FAC contributions to B_H at Colaba are seen to increase in amplitude up to 06:30 GMT, then sharply decrease, mirroring the solar wind pressure on the magnetosphere and the motion of the magnetopause. The magnetospheric contribution can also be seen to reduce by 650 nT between 06:30 and 07:30 GMT, where it remains for the rest of the simulation.

Between the three different scenarios in this paper, we can infer the behaviour of the simulated ring current, and its role in the dip and recovery of the Colaba B_H . The dip (up to 06:30 GMT) appears in all three simulations, indicating that it is not due to a build up of the ring current. However, the magnetosphere clearly contributes more to B_H at Colaba when RCM is included as part of the simulation. When the magnetosphere was at its most compressed, there is a difference of around 250 nT between the B_H^{MAG} of the Scenario 1 and 3 simulations. This is possibly due to the nightside buildup of particles at this time (panel B of Figure 3). Despite this, the magnetosphere of Scenario 3 is still able

to produce around -800 nT by 06:30 GMT at Colaba without a ring current. The recovery also appears not be due to a ring current. Between 06:30 and 07:30, both Scenarios 1 and 3 show a recovery of around 500 nT in B_H^{MAG} . The difference between the two is that there is a continuous B_H contribution from the magnetosphere in Scenario 1 (where a ring current is formed then kept energised by the solar wind driver), whereas this is absent in Scenario 3.

The behaviour of the B_H^{MAG} in Scenario 2 shows how the simulated ring current would decay in the complete absence of solar wind drivers. This would appear to be too slow to account for the rapid recovery seen at Colaba (as it is simulated in our setup). While not modeled in the version of RCM used in our simulations, a critical loss mechanism in the ring current is charge exchange with geocoronal neutral hydrogen. In the present simulations, ring current populations are being injected deeply to low L-shells where the geocoronal density is high and, equivalently, the charge exchange loss rate will be high [Ilie *et al.*, 2013]. An inclusion of realistic charge exchange loss terms would drive additional losses not captured in the current model version, potentially improving the comparison to the Colaba magnetometer station.

4. Discussion

The extreme geomagnetic storm event simulated here offers possible insight for three questions regarding the Carrington event:

1. What mechanism could have caused the extreme dip and rapid recovery of B_H at Colaba?
2. What were the solar wind conditions that could have driven such an event?

3. What was the Dst of the event?

We will discuss each point here, followed by a brief discussion of where the simulation failed to reproduce Carrington event measurements.

4.1. Colaba B_H dip and recovery

For our simulation, the extreme dip and rapid recovery of B_H at Colaba (and indeed the low-latitude region of Earth at solar noon) was a combination of near-Earth magnetospheric currents and FACs. As the solar wind pressure increased to a peak of around 1,000 nPa, the magnetosphere was compressed, and the magnetopause was forced extremely close to the Earth. Adjacent to the magnetopause were symmetric regions of Westward current. These lobes of current led to a very negative B_N signal at low-latitudes at the dayside of the Earth. Coupled with current contributions from Region 1 FACs in the simulation (which connect the magnetosphere and ionosphere domains), the B_H signal at Colaba was negative enough to match the $-1,750$ nT dip measured in 1859.

The rapid recovery of B_H in our simulation appears to be mostly due to the expansion of the magnetopause (as the solar wind conditions are relaxed), taking the magnetospheric lobes of Westward current further away from the Earth. As the solar wind pressure reduces and the magnetopause retreats, the negative B_N contribution from FACs similarly decreases as well. For Scenario 1, the combination of these factors means that the recovery of B_H at Colaba between 06:30 GMT and 07:00 GMT (approximately $+1100$ nT) broadly matches the rapidity and amplitude of the recovery measured at Colaba in 1859.

As shown in the previous section, the role of the ring current in the rapid dip and recovery at the dayside of the Earth is minimal. Although there was a night-side build up of near-Earth particles which did contribute to the negative B_H at Colaba when RCM

was included (and the ring-current simulated), an approximation of the dip and recovery was reproduced when RCM was not included in the simulation. After around 07:30 GMT, the contribution from the magnetosphere in Scenario 1 is due almost entirely due to ring current, similar to normal large-scale geomagnetic storm events at low-latitudes. Without RCM, the signal at Colaba is underestimated after 07:30 GMT.

4.2. Solar Wind Driver

The solar wind conditions which drove our simulation were chosen to exert an extreme dynamic pressure upon the magnetosphere, in order to drive the scenario described above and emulate the B_H at Colaba in 1859. We chose this measured B_H time-series as the template for our synthetic solar wind time-series, so that the proximity of the magnetopause to Earth would mirror the dip and recovery of the historical time-series. For simplicity, the other solar wind conditions (B , n , T) also used the same template.

The peak values used in this simulation for the solar wind velocity, density and B_Z value are large, but not so that they are impossibly large. Maximum Earthward solar velocity equal to $2,500 \text{ km s}^{-1}$ has been measured before in the July 2012 CME [Ngwira *et al.*, 2013].

The solar wind density peaks at 96 cm^{-3} , which is unusually high, but lower than extreme densities which have been measured before in CME filaments [Tsurutani *et al.*, 2017]. The minimum solar wind B_Z was empirically scaled with the velocity to give -116 nT . This is an extreme value for a CME, only slightly smaller than the B_Z of Tsurutani & Lakhina [2014]’s ‘perfect’ CME scenario. The combination of solar wind velocity and B_Z gives a maximum interplanetary electric field equal to 290 mV m^{-1} , approximately 50% larger than the estimation given by Tsurutani *et al.* [2017]. The solar wind conditions used in this simulation could be considered an incremental improvement on previous simulations

of Carrington-type storms, as aspects of the storm were successfully recreated without requiring unrealistically high solar wind densities (as in *Ngwira et al.* [2014]). However, there remains many aspects of the solar wind conditions used that can be improved upon. This is evident when looking at measured magnetic field data at sites other than Colaba (this is explored further in Section 4.4).

Each of the solar wind components used to drive our simulation increase and decrease in intensity in concert. This adds to the geoeffectiveness of the solar wind (for example, solar wind pressure, which is a product of V_X and n , or the magnetic reconnection rate which is a product of V_X and B_Z). In reality, CMEs have a filament structure where the different components will peak at different times. Also effectively neglected in our simulation are the small-scale variations in the solar wind. Small-scale noise was added to the components, however the amplitude of this noise was arbitrarily chosen. Future simulations will include realistic noise and CME dynamics based on statistical analyses of historical solar wind conditions. Finally, little attention was paid to the solar wind conditions at the arrival of our CME, where we instead opted for a gradual increase in the intensity.

4.3. Dst of the Event

The Dst-index is an hourly global index calculated from four mid-latitude geomagnetic stations. It is one of a number of geomagnetic indices in use (such as AE, Kp, Ap, aa, etc.), each of which are designed to measure different aspects of geomagnetic disturbances. The Dst index is often used to determine the occurrence and length of geomagnetic storms, and is used as a proxy for the strength of the symmetric ring-current. However, Dst is affected by other storm-time phenomena, and reducing all of the global storm dynamics

to a single hourly Dst value (or minutely in SYM-H) is at best a simplification [Borovsky
& Shprits, 2017].

Despite this, the minimum Dst value for a storm event is commonly used as a simple
indicator of storm severity. Dst is also an often used metric in statistical studies to estimate
the intensity of extreme but infrequent geomagnetic events [Riley, 2012; Chapman et al.,
2020; Morina et al., 2019]. Recently, multiple large pre-1957 storms have been studied
and had quasi-Dst values calculated [Love et al., 2019, b; Bhaskar et al., 2020; Hayakawa
et al., 2020]. Finally, as outlined in Section 1, the Dst of the Carrington event itself has
been subject to much inquiry. For these reasons, we discuss the calculated Dst of our
simulated event.

As shown above, the extremely impulsive scenario outlined in this paper resulted in a
very asymmetrical B field at low-latitudes particularly when the magnetopause was at its
most compressed. In addition, the unusual signal at the dayside was not caused by the
ring-current, which the Dst series was devised to measure. This poses a problem when
attempting to classify the strength of the storm using the Dst index. In the SWMF, the
Dst value is calculated by summing the magnetic contribution from the magnetosphere
domain and the ionosphere to a point in the center of the Earth using the Biot-Savart
law [Liemohn et al., 2018]. In reality, the Dst index is calculated from four low-latitude
geomagnetic observatories with the following equation:

$$Dst(t) = \frac{1}{4} \sum_{i=1}^4 \frac{Dist_i}{\cos \lambda_i} \quad (2)$$

where $Dist_i$ is the ‘local disturbance’ at observatory i (the hourly B_H variation mi-
nus baseline and solar-quiet signal), and the λ_i term is the magnetic latitude of the i th

observatory [Love & Gannon, 2009]. The four sites currently used to calculate Dst are located at Hermanus, Kakioka, Honolulu and San Juan. The top panel in Figure 8 shows the location of these four observatories as green diamonds, overplotted on the maximum calculated B_H at all points for the duration of the simulation.

Substituting the SWMF B_H timeseries at each of these sites into Equation 2 instead of $Dist$, a quasi-Dst value was calculated. The magnetic latitude of each observatory (λ) was calculated for 1900 (as this is the earliest date for which magnetic coordinates can be calculated using the IGRF model). Although the distance between the GUFM calculated 1859 and 1900 North poles is approximately 140 km, this would minimally affect the Dst calculation for Equation 2. The resulting Dst for these four sites is shown in the bottom panel of Figure 8 in green, and for the first 7 hours of simulation, the minimum Dst was -449 nT. Next, the longitudinal position of each of these sites was shifted in 1° increments, and this Dst calculation was repeated, giving 360 Dst timeseries. The positions of these shifted sites which resulted in the minimum calculated Dst are shown as red stars in the top panel of Figure 8. When the sites were located at these positions, the minimum calculated Dst was -1303 nT. This time-series is shown in red in the bottom panel of Figure 8

As can be seen in this figure, the longitudinal position of the Dst recording sites has a significant effect on the magnitude of the calculated Dst, particularly during the first few hours of the disturbance. In our impulsive storm scenario, the high pressure solar-wind forces the magnetopause and magnetospheric currents very close to the dayside of the Earth, leading to a localised low-latitude B_H signal. As pointed out in *Cid et al.* [2015],

for B_H spikes that are large in amplitude but spatially localized, a calculated Dst index may not accurately reflect the intensity of a storm.

Using the process outlined above, we have a range of Dst-equivalent values with which we can describe our simulated storm. The Dst calculated using the actual Dst observatories results in a minimum Dst = -449 nT. This value is on par with the Dst for the 20-21 November 2003 storm (Dst = -422 nT). The simulated storm here is clearly more intense than the November 2003 storm in terms of solar wind conditions (the 2003 event had minimum $V_X = -751$ km s $^{-1}$, $B_Z = -52.33$ nT and maximum $n = 28.7$ cm $^{-3}$), and low-latitude B_H (no INTERMAGNET site with magnetic latitude $< 30^\circ$ recorded a ΔB_H larger than 760 nT during the 2003 event). Figure 9 shows the maximum ΔB_H for every latitude in the SWMF simulation (orange line), ΔB_H at interpolated INTERMAGNET sites (blue dots) and INTERMAGNET sites during the 20-21 November 2003 storm (green dots). From this, the SWMF simulation can be seen to have much larger ΔB_H at most latitudes, especially less than 25° from the equator. This highlights both the potential problem with using Dst to quantify the intensity of a geomagnetic storm, and the unusual nature of the simulated storm.

The SWMF calculated Dst for the simulation (minimum Dst = -989 nT) and the maximum calculated Dst with the recording sites shifted longitudinally (minimum Dst -1303 nT) are within or near the spread of Dst estimates for the Carrington event in the literature. These are between -850 and -1160 nT for empirical estimates and between -625 and -1160 nT for modelled estimates (see *Cliver & Dietrich* [2013] and references within). This is unsurprising given that the previously calculated Dst values use the 1859 Colaba dataset, which our simulation emulates.

The Dst of a storm event can be used as an input for calculating the drag effects on satellites during geomagnetic storms [Prolss, 2011; Emmert, 2015; Zesta & Huang, 2016]. Oliveira et al. [2020] used recreated Dst estimates for different large-scale historical superstorms, and calculated the magnitude of satellite drag effects. Given the unusual nature of our Carrington event simulation, (where the calculated Dst is particularly not a good proxy for the ring current) we believe that our Carrington event simulation is not suitable for these calculations.

4.4. A Realistic Description of the Carrington Event?

The main focus of this study was to emulate the extraordinary B_H dataset at Colaba using a physics-based simulation. The solar wind drivers used in the simulation were tailored to force the magnetopause close to the Earth and then rapidly move away. This resulted in the intense dip and rapid recovery of B_H at Colaba, and was achieved using extreme but not unreasonable solar wind maxima conditions.

Although the Colaba dataset is the only known B_H time-series from the Carrington event that both had a reasonably high cadence and remained in-scale, other observatories were recording the horizontal magnetic field at the time. Three of these observatories were at Rome (41.9°N, 12.49°E), St. Petersburg (59.93°N, 30.36°E) and Barnaul (53.35°N, 83.78°E). Similar to Figure 4, we can interpolate B_H at these locations and compare with the measured values. The comparison between measured and simulated B_H at these three sites is shown in the top row of Figure 10.

It is clear that the measured B_H time-series at these three sites are not recreated as well as for Colaba in the simulation. In the case of Rome, there was a reported off-scale

deviation of approximately 3,000 nT between 06:00 and 06:30 GMT. Allowing for timing errors, the amplitude of the simulated dip at Rome is less than 1,000 nT, a significant underestimate of the total ΔB_H . *Blake et al.* [2020] suggests that the extremely large deviation measured at Rome indicates that it was beneath the auroral oval on the morning of the 2 September 1859. From panel B of Figure 5, the magnetic effects of the ionosphere can be seen to reach low latitudes equivalent to Rome (near Central America on the nightside for example), but it does not appear to reach Rome for our simulation.

In the case of St. Petersburg and Barnaul, measurements were taken only once every hour. While this makes it difficult to directly compare to the 1-min simulated data (see *Viljanen et al.* [2014]), at both sites there are clearly large positive B_H deviations in the time-series towards the beginning of the storm (+500 nT at St. Petersburg, and +720 nT at Barnaul). Neither of these positive deviations are recreated in our simulation.

Indeed, the simulated B_H at each of the three sites follow much the same shape, dipping and recovering much like the simulated B_H at Colaba. However, as shown in the bottom panel of Figure 10, the ratios of the B_H contributions from the magnetosphere, ionosphere and FACs are different for each site.

While our simulation can emulate the Colaba B_H dataset well, from these three examples, it is clear that our simulation is not a good global recreation of the Carrington event. This is to be expected, particularly given the simplifications in our chosen solar wind profile (see Section 4.2), as well as the physical limitations and caveats of the SWMF model, especially when simulating such an extreme event.

The particular configuration of SWMF that we have used for this study (BATS-R-US, RCM and RIM) have been shown before to be capable of reproducing surface magnetic

fields for other storm events [Welling, 2019]. However, there are a number of aspects of the simulation that could be appraised for future simulations. The Biot-Savart approximation used in our simulations is a free-space implementation, which does not account for conducting bodies or boundaries. For a simulation with significant short-lived magnetospheric current structures near the Earth (such as the event in this paper), the application of the Biot-Savart approximation could be investigated.

The resolution of the cells closest to the Earth can also affect the calculated surface magnetic fields. While our simulation used cells near the Earth sized at $1/16 R_E$, it is unclear if these were small enough to adequately resolve phenomena such as bursty bulk flows (BBFs) and other substorm dynamics. While our simulation was primarily concerned with the ground magnetic contributions from large-scale structures, this is an avenue that should be explored in the future for more physically accurate simulations, particularly when analysing the ground magnetic field at auroral latitudes.

The RCM used for this simulation used a fixed composition of 0.9 : 0.1 for $H^+ : O^+$. Simplifications such as these can be changed for future simulations.

5. Conclusion

Using the SWMF, the quick dip and rapid recovery of the measured B_H at Colaba during the Carrington event were recreated during a large geomagnetic storm scenario. This was achieved by using an extremely impulsive ($\sim 1,000$ nPa) solar wind driver, which forced the magnetopause to within $2.3 R_E$ of the Earth. The main contributions to the extremely negative B_H at Colaba were due to the proximity of Westward electric currents adjacent to the magnetopause, as well as from strong Region 1 FACs. As the solar wind

pressure abated and the magnetopause moved away from the Earth, the quick recovery of B_H at low-latitudes was primarily due to the motion of the Westward electric currents in the near-Earth dayside magnetosphere. For our simulation, the ring current did not appear to play a significant role in the Colaba dip and recovery.

The solar wind amplitudes needed to drive such a scenario were extreme, but not unrealistic, with maximum $V_X = -2,500 \text{ kms}^{-1}$, $B_Z = -127 \text{ nT}$ and maximum $n = 95 \text{ cm}^{-3}$. These peak values for V_X and n are smaller than has been measured before in the solar wind. The Dst calculated for this event by the SWMF had a minimum of -989 nT . However, given the localized nature of the low-latitude dayside B_H during the storm, the longitudinal location of Dst recording sites would have a marked effect on the calculated Dst. Depending on the timing of this storm, minimum calculated Dst could range from -457 nT to -1087 nT .

While the storm scenario in this study was able to reproduce the B_H at Colaba, it performed significantly less well when recreating the B_H at other geomagnetic observatories. It would be unreasonable to declare the geomagnetic storm scenario in this paper as being an accurate replication of the magnetospheric and ionospheric conditions during the Carrington event. Rather, it highlights a possible mechanism for the unusual dip and recovery of B_H at Colaba using (somewhat) realistic solar wind conditions. That is to say, the simulated low-latitude dayside B_H which emulated the Colaba 1859 dataset is heavily dependent on the location of the magnetopause during this extreme storm scenario.

This study should be viewed as an initial step in simulating the Carrington event, where a tailor-made simulation was tweaked to reproduce the extraordinary Colaba B_H dataset. By using different combinations of SWMF modules parameters and by particularly varying

the solar wind inputs, we may be able to better recreate and understand the global processes that occurred during the extraordinary 1859 Carrington event storm.

Acknowledgments. The Colaba B_H data were digitised from *Tsurutani et al.* [2003] using the WebPlotDigitizer software (<https://automeris.io/WebPlotDigitizer/>). The Bar-
naul and St. Petersburg B_H data were taken from *Nevanlinna* [2008]. Rome B_H data were taken from *Blake et al.* [2020]. Datasets used to produce the images in this paper can be found at <https://doi.org/10.5281/zenodo.4534660>. The complete run folders for each SWMF simulation can be requested from the Community Coordinated Modeling Center (<https://ccmc.gsfc.nasa.gov/index.php>). The results presented in this paper rely on data collected at magnetic observatories. We thank the national institutes that support them and INTERMAGNET for promoting high standards of magnetic observatory practice (www.intermagnet.org). The SWMF simulations were run on the Discover supercomputing cluster at NASA's Center for Climate Simulation (HEC-SMD-18-1749). Data were also obtained from the SuperMAG database (<http://supermag.jhuapl.edu/info/?page=faq>). This work was supported by the NASA's Living With a Star program (17-LWS17.2-0042), and the Electric Power Research Institute (EPRI SAA5-2017-4-R26568). Dr. Welling is supported by National Science Foundation award ICER-1663770. We thank the reviewers for their constructive comments.

References

Allen, J., Frank, L., Sauer, H., Reiff, P., (1989) Effects of the March 1989 Solar Activity, *EOS Transactions AGU*, 70(46) 1479-1488 <https://doi.org/10.1029/89EO00409>

- 674 Aplin, K.L., Harrison, R.G., (2014) Atmospheric electric fields during the Carrington
675 flare., *Astron Geophys*, 55 32-37 doi:10.1093/astrogeo/atu218
- 676 Bhaskar, A., Hayakawa, H., Oliveira, D.M., Blake, S.P., Silverman, S.M., Ebihara, Y.,
677 (2020) An analysis of the Trouvelots Auroral Drawing on 1/2 March 1872 : Plausi-
678 ble Evidence for Recurrent Geomagnetic Storms, *J. Geophys. Res. Space Physics*, 125
679 e2020JA028227 <https://doi.org/10.1029/2020JA028227>
- 680 Blake, S.P., Pulkkinen, A., Schuck, P.W., Nevanlinna, H., Reale, O., Veenad-
681 hari, B., Mukherjee, S., (2002) Magnetic Field Measurements from Rome dur-
682 ing the August-September 1859 Storms, *J. Geophys. Res.*, 125 e2019JA027336
683 <https://doi.org/10.1029/2019JA027336>
- 684 Blake, S.P., Pulkkinen, A., Schuck, P.W., Gloer, A., Tóth, G., (2020) Es-
685 timating Maximum Extent of Auroral Equatorward Boundary using Historical
686 and Simulated Surface Magnetic Field Data, *J. Geophys. Res. Space Physics*,
687 <https://doi.org/10.1029/2020JA028284>
- 688 Bolduc, L., (2002) GIC observations and studies in the Hydro-Quebec power system, *J.*
689 *Atmos. Sol.-Terr. Phys.*, 64 1793–1802 [https://doi.org/10.1016/S1364-6826\(02\)00128-](https://doi.org/10.1016/S1364-6826(02)00128-1)
690 1
- 691 Borovsky, J.E., Shprits, Y.Y., (2017) Is the Dst Index Sufficient to Define
692 All Geospace Storms?, *J. Geophys. Res. Space Physics*, 122 11,543–11,547
693 <https://doi.org/10.1002/2017JA024679>
- 694 Boteler, D.H., (2006) The super storms of August/September 1859 and
695 their effects on the telegraph system, *Adv. in Space Res.*, 38 159–172
696 <https://doi.org/10.1016/j.asr.2006.01.013>

- Boteler, D.H., (2019) A Twenty-First Century View of the March 1989 Magnetic Storm, *Space Weather*, 17(10) 1427-1441 <https://doi.org/10.1029/2019SW002278>
- Burton, R.K., McPherron, R.L., Russell, C.T., (1975) An empirical relationship between interplanetary conditions and Dst, *J. Geophys. Res.*, 80 4204-4211 <https://doi.org/10.1029/JA080i031p04204>
- Cid, C., Saiz, E., Guerrero, A., Palacios, J., Cerrato, Y., (2015) A Carrington-like geomagnetic storm observed in the 21st century, *J. Space Weather Space Clim.*, 5 A16 <https://doi.org/10.1051/swsc/2015017>
- Carrington, R., (1859) Singular Appearance in the Sun, *Monthly Notices Royal Astron. Soc.*, 20 13-15
- Chapman, S.C., Horne, R.B., Watkins, N.W., (2020) Using the aa Index Over the Last 14 Solar Cycles to Characterize Extreme Geomagnetic Activity, *Geophysical Research Letters*, 47 e2019GL086524 <https://doi.org/10.1029/2019GL086524>
- Clark, S., (2007) Astronomical fire: Richard Carrington and the solar flare of 1859, *Endeavour*, 31(3) 104-109 <https://doi.org/10.1016/j.endeavour.2007.07.004>
- Cliver, E.W., Dietrich, W.F., (2013) The 1859 space weather event revisited: limits of extreme activity, *J. Space Weather Space Clim.*, 3 A31 <https://doi.org/10.1051/swsc/2013053>
- Curto, J.J., (2020) Uncertainty in hourly mean data from classical magnetometers, *Earth, Planets and Space*, 71(139) 1-14 <https://doi.org/10.1186/s40623-019-1119-2>
- De Zeeuw, D.L., Gombosi, T.I., Groth, C.P.T., Powell, K.G., Stout, Q.F., (2000) An adaptive MHD method for global space weather simulations, *IEEE Transactions on Plasma Science*, 28 1956-1965 <https://doi.org/10.1109/27.902224>

- 720 De Zeeuw, D.L., Sazykin, S., Wolf, R.A., Gombosi, T.I., Ridley, A.J., Toth, G., (2004)
721 Coupling of a global MHD code and an inner magnetospheric model: Initial results,
722 *Journal of Geophysical Research*, *109* A12219 <https://doi.org/10.1029/2003JA010366>
723 Emmert, J.T., (2015), Thermospheric mass density: A review, *Adv. Space Res.*, *56* 5
724 <https://doi.org/10.1016/j.asr.2015.05.038>
725 González-Esparza, J.A., Cuevas-Cardona, M.C., (2018) Observations of LowLatitude Red
726 Aurora in Mexico During the 1859 Carrington Geomagnetic Storm, *Space Weather*, *16*
727 6 <https://doi.org/10.1029/2017SW001789>
728 Gonzalez, W.D., Clúa de Gonzalez, A.L., Dal Lago, A., Tsurutani, B.T., Ar-
729 ballo, J.K., Lakhina, G.K., Buti, B., Ho, C.M, Wu, S.-T.(1998) Magnetic cloud
730 field intensities and solar wind velocities, *Geophysical Research Letters*, *25* 963-966
731 <https://doi.org/10.1029/98GL00703>
732 Gonzalez, W.D., Echer, E., Tsurutani, B.T., Clua de Gonzalez, A.L., Dal Lago, A., (2011)
733 Interplanetary Origin of Intense, Superintense and Extreme Geomagnetic Storms, *Space*
734 *Sci. Rev.*, *158* 69-89 <https://doi.org/10.1007/s11214-010-9715-2>
735 Green, J.L, Boardsen, S., (2006) Duration and extent of the great auroral storm of 1859,
736 *Adv. Space Res.*, *38* 130-135 <https://doi.org/10.1016/j.asr.2005.08.054>
737 Haiducek, J.D., Welling, D.T., Ganushkina, N.Y., Morley, S.K., Ozturk, D.S.,
738 (2017), SWMF Global Magnetosphere Simulations of January 2005: Geomag-
739 netic Indices and Cross-Polar Cap Potential, *Space Weather*, *15* 1567-1587
740 <https://doi.org/10.1002/2017SW001695>
741 Hayakawa, H., Ebihara, Y., Willis, D.M., et al., (2019), Temporal and Spatial Evolutions
742 of a Large Sunspot Group and Great Auroral Storms around the Carrington Event in

1859, *Space Weather*, 869:57 <https://doi.org/10.1029/2019SW002269>

Hayakawa, H., Ribeiro, P., Vaquero, J.M., Gallego, M.C., Knipp, D.J., Mekhaldi, F., Bhaskar, A., Oliveira, D.M., Notsu, Y., Carrasco, V.M.S., Caccavari, A., Veenadhari, B., Mukherjee, S., Ebihara, Y., (2020), The Extreme Space Weather Event in 1903 October/November: An Outburst from the Quiet Sun. *The Astrophysical Journal Letters*, <https://doi.org/10.3847/2041-8213/ab6a18>

Hodgson, R., (1859), On a curious Appearance seen in the Sun, *Monthly notices of the RAS*, 20:1 15-16 <https://doi.org/10.1093/mnras/20.1.15a>

Hoffman, R.A., Cahill, L.J., Anderson, R.R., Maynard, N.C., Smith, P.H., Fritz, T.A., Williams, D.J., Konradi, A., Gurnett, D.A., (1975), Explorer 45 (S³-A) observations of the magnetosphere and magnetopause during the August 4-6, 1972, magnetic storm period, *Journal of Geophys. Res.*, 80(31) 4287-4296 <https://doi.org/10.1029/JA080i031p04287>

Ilie, R., Skoug, R. M., Funsten, H. O., Liemohn, M. W., Bailey, J. J., & Gruntman, M. (2013). The impact of geocoronal density on ring current development, *Journal of Atmospheric and Solar-Terrestrial Physics*, 99 92-103 <https://doi.org/10.1029/JA080i031p04287>

Jackson, A., Jonkers, A.R.T., Walker, M.R., (2018), Four centuries of geomagnetic secular variation from historical records, *Philos. Trans. Royal Soc. A*, 358 957-990 <https://doi.org/10.1098/rsta.2000.0569>

Jacob, W.S., (1884), Magnetical Observations made at the honorable East India Company's Observatory at Madras in the years 1851-1855, *The Lawrence Asylum Press*,

- Janhunen, P., Palmroth, M., Laitinen, T., Honkonen, I., Juusola, L., Facsko, G.,
Pulkkinen, T.I., (2012), The GUMICS-4 global MHD magnetosphere-ionosphere cou-
pling simulation, *Journal of Atmospheric and Solar-Terrestrial Physics*, 80 48-59
<https://doi.org/10.1016/j.jastp.2012.03.006>
- Keika, K., Ebihara, Y., Kataoka, R., (2015), What caused the rapid recovery of the
Carrington storm?, *Earth, Planets and Space*, 67:65 <https://doi.org/10.1186/s40623-015-0234-y>
- Kimball, D.S., (1960), A study of the Aurora of 1859, *Scientific Report No. 6, University
of Alaska* <http://hdl.handle.net/11122/3607>
- Koons, H.C., Fennell, J.F., (2006), Space Weather effects on com-
munication satellites *URSI Radio Science Bulletin*, Vol 2006 316
<https://doi.org/10.23919/URSIRSB.2006.7909358>
- Kumar, S., Veenadhari, B., Tulasi Ram, S., Selvakumaran, R., Mukherjee, S.,
Singh, R., Kadam, B.D., (2015), Estimation of interplanetary electric field con-
ditions for historical geomagnetic storms, *J. Geophys. Res. Space Physics*, 120
<https://doi.org/10.1002/2015JA021661>
- Li, X., Temerin, M., Wygant, J.R., Hudson, M.K., Blake, J.B., (1993) Simulation of the
prompt energization and transport of radiation belt particles during the March 24, 1991
SC, *Geophys. Res. Letters*, 20 2423-2426 <https://doi.org/10.1029/93GL02701>
- Li, X., Temerin, M., Tsurutani, B.T., Alex, S., (2006) Modeling of 1-
2 September 1859 super magnetic storm, *Adv. Space Res.*, 38 273-279
<https://doi.org/10.1016/j.asr.2005.06.070>

- Liemohn, M., Ganushkina, N.Y., De Zeeuw, D.L., Rastaetter, L., Kuznetsova, M., Welling, D.T., Toth, G., Ilie, R., Gombosi, T.I., van der Holst, B., (2018) Real-Time SWMF at CCMC: Assessing the Dst Output From Continuous Operational Simulations *Space Weather*, *16* 1583–1603 <https://doi.org/10.1029/2018SW001953>
- Loomis, E., (1861), On the great auroral exhibition of Aug. 28th to Sept. 4th, 1859 and on auroras generally; Article 4, *Am. J. Sci.*, *2*, *32*, <https://doi.org/10.2475/ajs.s2-32.96.318>
- Love, J.J., Gannon, J.L., (2009) Revised Dst and the epicycles of magnetic disturbance: 1958-2007, *Ann. Geophys.*, *27* 3101-3131 <https://doi.org/10.5194/angeo-27-3101-2009>
- Love, J.J., Hayakawa, H., Cliver, E.W., (2019), Intensity and Impact of the New York Railroad Superstorm of May 1921, *Space Weather*, *17* <https://doi.org/10.1029/2019SW002250>
- Love, J.J., Hayakawa, H., Cliver, E.W., (2019), On the Intensity of the Magnetic Superstorm of September 1909, *Space Weather*, *17* 37-45 <https://doi.org/10.1029/2018SW002079>
- Lyon, J.G., Fedder, J.A., Mobarry, C.M., (2004), The Lyon-Fedder-Mobarry (LFM) global MHD magnetospheric simulation code, *Journal of Atmospheric and Solar-Terrestrial Physics*, *66* 1333–1350 <https://doi.org/10.1016/j.jastp.2004.03.020>
- Manchester IV, W.B., Ridley, A.J., Gombosi, T.I., DeZeeuw, D.L., (2005), Modeling the Sun-to-Earth propagation of a very fast CME, *Advances in Space Research*, *38* <https://doi.org/10.1016/j.asr.2005.09.044>
- Morina, D., Serra, I., Puig, P., Corral, A., (2017), Probability estimation of a Carrington-like geomagnetic storm, *Nature Scientific Reports*, *9*:2393 <https://doi.org/10.1038/s41598-019-38918-8>

- 809 Nevanlinna, H., Häkkinen, L., (2010), Results of Russian geomagnetic observatories
810 in the 19th century: magnetic activity, 1841-1862, *Ann. Geophys.*, *28* 917–926
811 <https://doi.org/10.5194/angeo-28-917-2010>
- 812 Nevanlinna, H., (2008), On geomagnetic variations during the August-September storms
813 of 1859, *Adv. in Space Res.*, *42* 171-180 <https://doi.org/10.1016/j.asr.2008.01.002>
- 814 Ngwira, C.M, Pulkkinen, A., Leila Mays, M., Kuznetsova, M., Galvin, A.B., Simunac,
815 K., Baker, D.N., Li, X., Zheng, Y., Gloer, A., (2013), Simulation of the 23 July 2012
816 extreme space weather event: What if this extremely rare CME was Earth directed?,
817 *Space Weather*, *11* 671–679 <https://doi.org/10.1002/2013SW000990>
- 818 Ngwira, C.M, Pulkkinen, A., Kuznetsova, M., Gloer, A., (2014), Model-
819 ing extreme "Carrington-type" space weather events using three-dimensional
820 global MHD simulations, *J. Geophys. Res. Space Physics*, *119* 4456–4474
821 <https://doi.org/10.1002/2013JA019661>
- 822 O'Brien, T.P, McPherron, R.L. (2000), An empirical phase space analysis of ring current
823 dynamics: solar wind control of injection and decay, *J. Geophys. Res.*, *105* 7707–7719
824 <https://doi.org/10.1029/1998JA000437>
- 825 Okoh, D., Okoro, E., (2020), On the Relationships Between Sunspot Number and Solar
826 Radio Flux at 10.7 Centimeters, *Solar Phys.*, *295:1* [https://doi.org/10.1007/s11207-](https://doi.org/10.1007/s11207-019-1566-8)
827 019-1566-8
- 828 Oliveira, D.M., Zesta, E., Schuck, P.w., Sutton, E.K. (2017), Thermosphere global time
829 response to geomagnetic storms caused by coronal mass ejections, *J. Geophys. Res. Space*
830 *Physics*, *122* 10 <https://doi.org/10.1002/2017JA024006>

- Oliveira, D.M., Samsonov, A.A., (2018), Geoeffectiveness of interplanetary shocks controlled by impact angles: A review., *Adv. in Space Res.*, 61(1) 1-44
<https://doi.org/10.1016/j.asr.2017.10.006>
- Oliveira, D.M., Zesta, E., (2019), Satellite Orbital Drag During Magnetic Storms, *Space Weather*, 17 1510-1533 <https://doi.org/10.1029/2019SW002287>
- Oliveira, D.M., Zesta, E., Hayakawa, H., Bhaskar, A., (2020), Estimating satellite orbital drag during historical magnetic superstorms, *Accepted for publication by Space Weather*, <https://agupubs.onlinelibrary.wiley.com/doi/abs/10.1029/2020SW002472>
- Oughton, E.J., Skelton, A., Horne, R.B., Thomson, A.W.P., Gaunt, C.T. (2017), Quantifying the daily economic impact of extreme space weather due to failure in electricity transmission infrastructure, *Space Weather*, 15(1) 65-83
<https://doi.org/10.1002/2016SW001491>
- Powell, K.G., Roe, P.L., Linde, T.J., (1999), A solution-adaptive upwind scheme for ideal magnetohydrodynamics, *Journal of Computational Physics*, 154 284-309
<https://doi.org/10.1006/jcph.1999.6299>
- Pulkkinen, A., Rastatter, L., Kuznetsova, M., Singer, H., Balch, C., Weimer, D., Toth, G., Ridley, A., Gombosi, T., Wiltberger, Raeder, J., Weigel, R., (2013), Community-wide validation of geospace model ground magnetic field perturbation predictions to support model transition to operations, *Space Weather*, 11 369-385
<https://doi.org/10.1002/swe.20056>
- Pulkkinen, A. et al., (2017), Geomagnetically induced currents: Science, engineering and applications readiness, *Space Weather*, 15 828-856 <https://doi.org/10.1002/2016SW001501>

- 853 Prölss, G.W., (2011), Density Perturbations in the Upper Atmosphere Caused
854 by the Dissipation of Solar Wind Energy, *Surveys in Geophysics*, 32 101-195
855 <https://doi.org/10.1007/s10712-010-9104-0>
- 856 Ridley, A.J., Gombosi, T.I., DeZeeuw, D.L. (2004), Ionospheric control of the magne-
857 tosphere: conductance, *Ann. Geophys*, 22 567-584 [https://doi.org/10.5194/angeo-22-567-](https://doi.org/10.5194/angeo-22-567-2004)
858 2004
- 859 Riley, P., (2012), On the probability of occurrence of extreme space weather events, *Space*
860 *Weather*, 10 S02012 <http://dx.doi.org/10.1029/2011SW000734>
- 861 Rudd, J.T., Oliveira, D.M., Bhaskar, A., Halford, A. (2019), How do interplanetary shock
862 impact angles control the size of the geoeffective magnetosphere?, *Adv. in Space Res.*,
863 63(1) 317-326 <https://doi.org/10.1016/j.asr.2018.09.013>
- 864 Shea, M.A., Smart, D.F., (2006), Compendium of the eight articles on the "Carrington
865 Event" attributed to or written by Elias Loomis in the American Journal of Science,
866 1859-1861, *Adv. in Space Research*, 38 313-385 <https://doi.org/10.2475/ajs.s2-32.96.318>
- 867 Siscoe, G., Crooker, N.U., Clauer, C.R. (2006), Dst of the Carrington storm of 1859, *Adv.*
868 *in Space Research*, 38 173-179 <https://doi.org/10.1016/j.asr.2005.02.102>
- 869 Toffoletto, F., Sazykin, S., Spiro, R., Wolf, R., (2003) Inner Magnetospheric
870 Modeling with the Rice Convection Model, *Space Science Reviews*, 107 175-196
871 <https://doi.org/10.1023/A:1025532008047>
- 872 Tóth, G. et al., (2003) Space Weather Modeling Framework: A new tool for the space
873 science community, *J. Geophys. Res.*, 110 A12226 <https://doi.org/10.1029/2005JA011126>
- 874 Tóth, G. et al., (2012) Adaptive numerical algorithms in space weather modeling, *Journal*
875 *of Computational Physics*, 231 <https://doi.org/10.1016/j.jcp.2011.02.006>

- 876 Tsurutani, B.T., Gonzalez, W.D., Lakhina, G.S., Alex, S., (2003) The ex-
877 treme magnetic storm of 1-2 September 1859, *J. Geophys. Res.*, *108* A7
878 <https://doi:10.1029/2002JA009504>
- 879 Tsurutani, B.T., Lakhina, G.S., (2014) An extreme coronal mass ejection and
880 consequences for the magnetosphere and Earth, *Geophys. Res. Lett.*, *41* 287-292
881 <https://doi:10.1002/2013GL058825>
- 882 Tsurutani, B.T., Lakhina, G.S., Echer, E., Hajra, R., Nayak, C., Mannucci, A.J.,
883 Meng, X., (2017) Comment on "Modeling Extreme "Carrington-Type" Space Weather
884 Events Using Three-Dimensional Global MHD Simulations" by C.M. Ngwira, A.
885 Pulkkinen, M. M. Kuznetsova and A. Gloer, *J. Geophys. Res.*, *123* 1388-1392
886 <https://doi:10.1002/2017JA024779>
- 887 Valach, F., Hejda, P., Revallo, M., Bochníček, J. (2019), Possible role of auro-
888 ral oval-related currents in two intense magnetic storms recorded by old mid-
889 latitude observatories Clementinum and Greenwich, *J. Space Weather Space Clim.*, *9*
890 <https://doi:10.1051/swsc/2019008>
- 891 Viljanen, A., Myllys, M., Nevanlinna, H., (2014), Russian geomagnetic recordings in
892 1850-1862 compared to modern observations, *J. Space Weather Space Clim.*, *4*, A11
893 <https://doi:10.1051/swsc/2014008>
- 894 Yu, Y., Ridley, A.J., Welling, D.T., Tth, G. (2010). Including gap region field-aligned
895 currents and magnetospheric currents in the MHD calculation of ground-based magnetic
896 field perturbations, *J. Geophys. Res.*, *115*, A8 <https://doi.org/10.1029/2009JA014869>
- 897 Yu, Y., Ridley, A.J. (2008), Validation of the space weather model-
898 ing framework using ground-based magnetometers, *Space Weather*, *6* 5

<https://doi.org/10.1029/2007SW000345>

Welling, D., Liemohn, M.W., (2014), Outflow in global magnetohydrodynamics as a function of a passive inner boundary source, *J. Geophys. Res. Space Physics*, 43-65

<https://doi.org/10.1002/2013JA019374>

Welling, D., (2019), Magnetohydrodynamic Models of B and Their Use in GIC Estimates, *Geomagnetically Induced Currents from the Sun to the Power Grid, Geophysical Monograph 244, First Edition* <https://doi.org/10.1002/9781119434412.ch3>

Welling, D., Love, J.J., Rigler, E.J., Oliveira, D.M., Komar, C.M.(2020), Numerical simulations of the geospace response to the arrival of a perfect interplanetary coronal mass ejection, *Space Weather*, <https://doi.org/10.1029/2020SW002489>

Zastenker, G.N., Temny, V.V., dUston, C., Bosqued, J.M., (1978), The form and energy of the shock waves from the solar flares of August 2, 4 and 7, *J. Geophys. Res.*, 83 1035-1041

Zesta, E., Huang, C.Y., (2016), Satellite orbital drag *Space Weather Fundamentals, Chapter 18, CRC Press 1035-1041*

Zhao, H., Li, X., (2013), Modeling energetic electron penetration into the slot region and inner radiation belt, *J. Geophys. Res. Space Physics, CRC 118 6936-6945* <https://doi.org/10.1002/2013JA019240>

Figure 1. The SWMF grid used in the simulations. This grid had 5.89 million cells.

Figure 2. The horizontal magnetic field measurements taken at Colaba during the Carrington event (top panel), and the solar wind conditions used to drive the two simulation scenarios (bottom 5 panels). Solar wind conditions for Scenario 1 and 3 are in bold red, and for Scenario 2 are in blue. These conditions are southward IMF magnetic field (B_z), velocity (V_x), particle density, pressure and temperature. The shaded blue region is the time-period simulated. The Colaba data were digitised from Figure 3 of *Tsurutani et al.* [2003].

Figure 3. Top panels: the total current density in the near-Earth magnetosphere for three different times during the Scenario 1 simulation. The radial white, black and red lines show the closed, open and most poleward closed magnetic field lines. Below these are three panels that show pressure in the near-Earth simulation. Note: each colorbar has a different scale. Bottom two panels show the calculated magnetopause standoff distance for Scenario 1 (red) and Scenario 2 (blue), and the SWMF calculated Dst for both simulations. The dashed vertical lines correspond to the times of the three magnetosphere snapshots in the top panels.

Figure 4. The measured and simulated B_H at Colaba for the two Carrington event scenarios, and the run with no RCM component. Top panels compare the measured historical (green) and SWMF simulated (red) timeseries. The bottom panels shows the magnetospheric (purple, B_H^{MAG}), Birkeland FAC (black, B_H^{FAC}) and ionospheric (blue, B_H^{IONO}) contributions to the SWMF timeseries. In addition, the solar wind ram pressure (P_{SW}) is overplot as a dotted green line. Panels A and D are for Scenario 1, B and E are for Scenario 2, and C and F are for Scenario 3 (without RCM)

Figure 5. The surface magnetic field and its contributions from SWMF at 06:30 GMT for Scenario 1. Panel A: the total $|B_H|$, Panel B: $|B_H|$ from the ionospheric domain, Panel C: $|B_H|$ from FACs, Panel D: $|B_H|$ from the magnetosphere. Note: panels A-D have different colorbar scales. Panel E: the B_N (Northward) component from FACs, Panel F: the B_N component from the magnetosphere. The colorbars of Panels E and F are limited to ± 1000 nT.

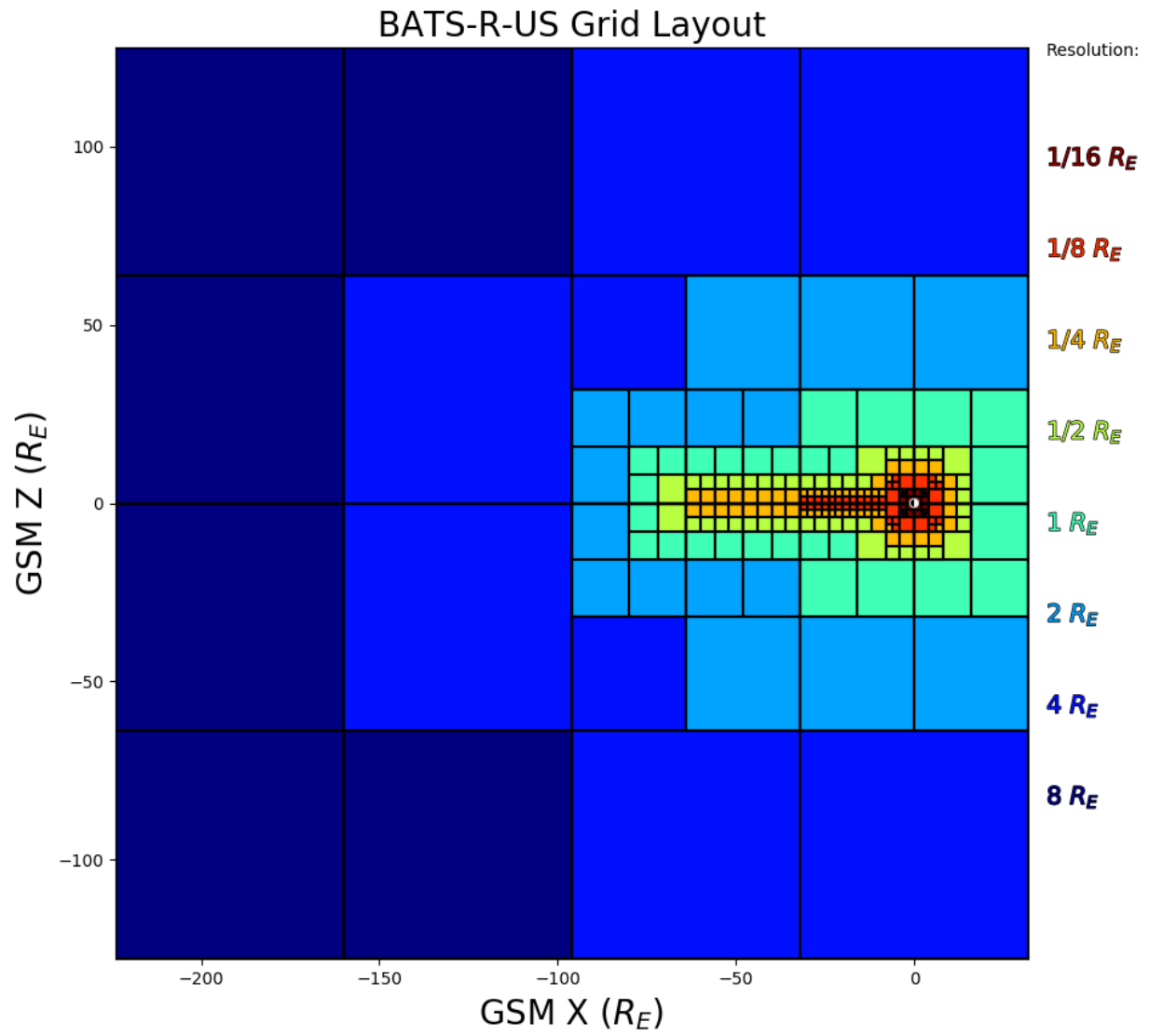
Figure 6. Top: The ionospheric radial current density in the Northern and Southern hemispheres at 06:30 GMT for Scenario 1. Middle and bottom: The Hall and Pedersen ionospheric conductances for the same time. These show a complicated broken-up pattern on the nightside.

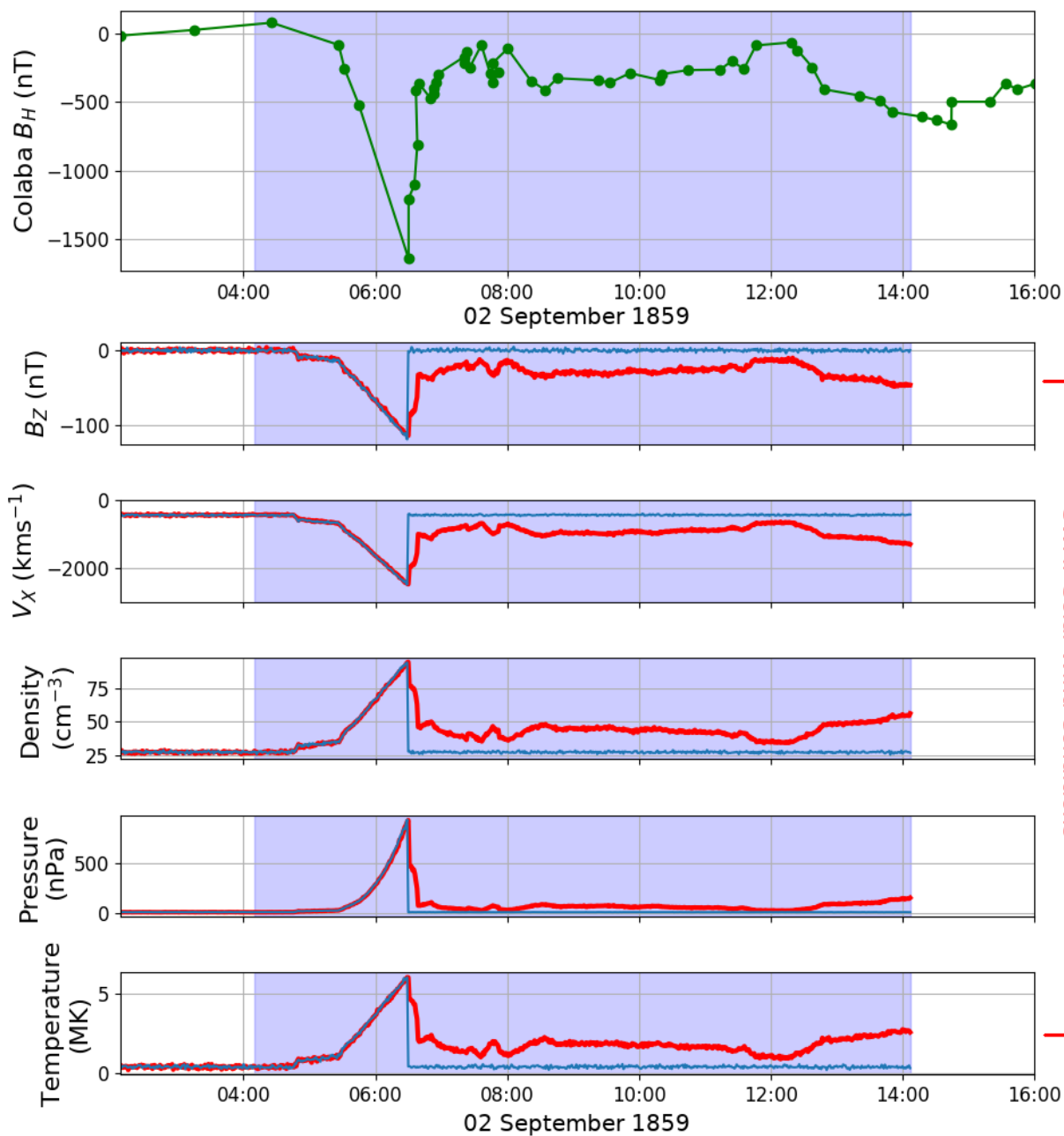
Figure 7. Azimuthal current density in two planes in the near-Earth magnetosphere at 06:30 GMT for Scenario 1. The Sun to the right of the plots. Left panel shows the $Y = 0 R_E$ XZ-plane. Right panel shows the $Z = 0.4 R_E$ XY-plane, and looks down upon the Northern hemisphere. Red regions will increase surface B_N at the Earth’s surface, and blue areas will decrease surface B_N .

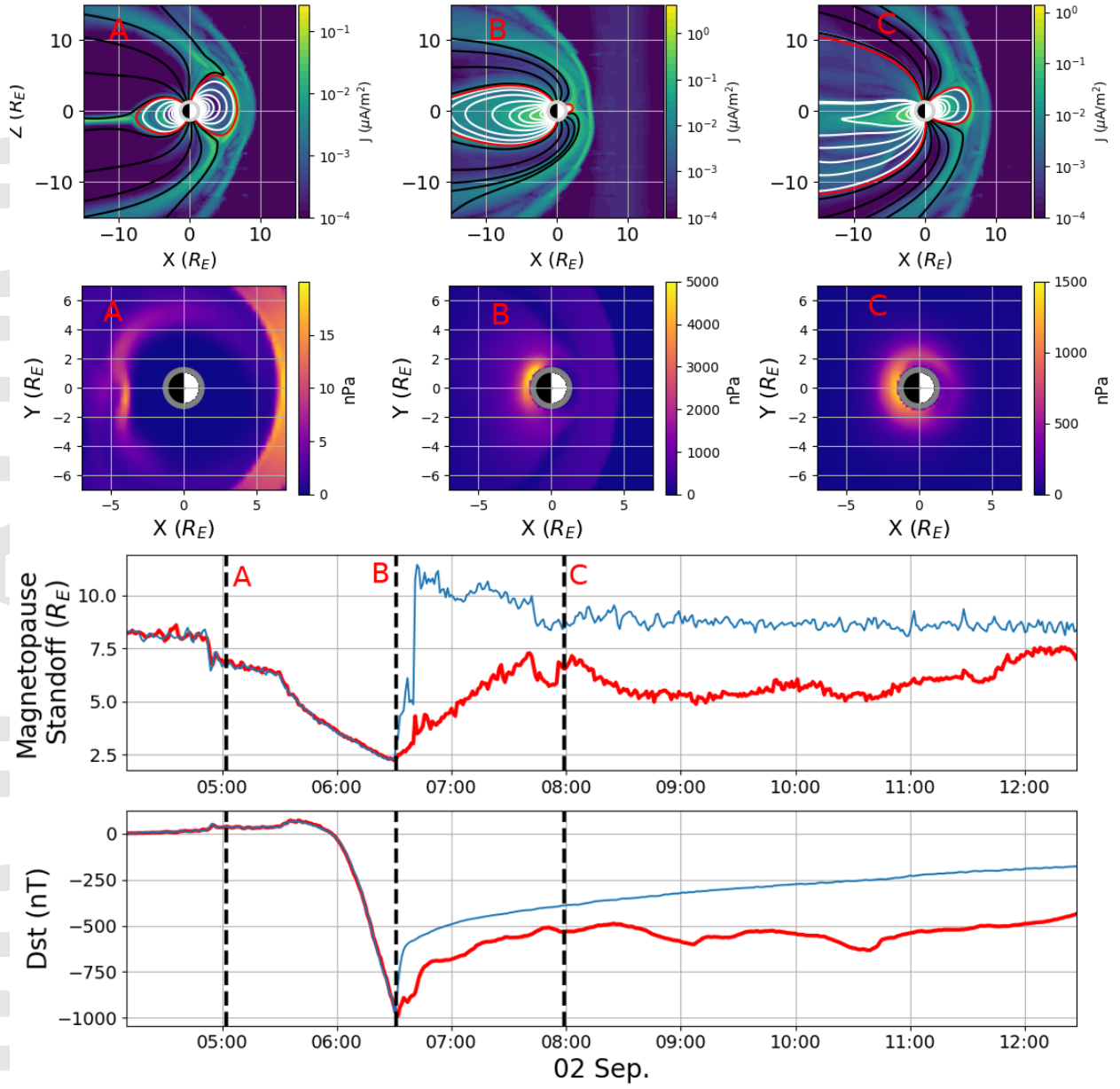
Figure 8. Top plot shows the maximum calculated B_H for the duration of Simulation 1. The actual location of the four observatories which are used to calculate Dst are shown as pink stars. The red stars show the shifted position of these observatories which will result in the most negative Dst calculation. Bottom plot shows the SWMF calculated Dst (black), the Dst calculated with real observatory positions (green) and the minimum calculated Dst (red).

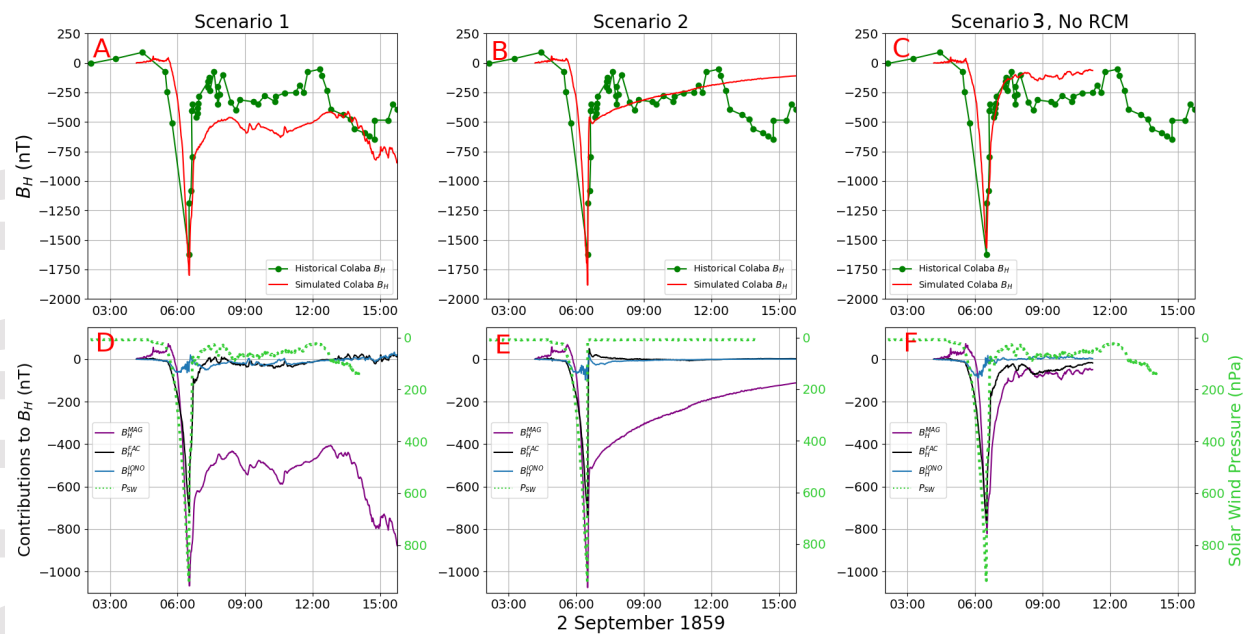
Figure 9. Maximum ΔB_H vs. geographic latitude for every latitude in the Carrington simulation (orange line), INTERMAGNET interpolated sites (blue dots) and INTERMAGNET sites during the 20-21 November 2003 storm (green dots).

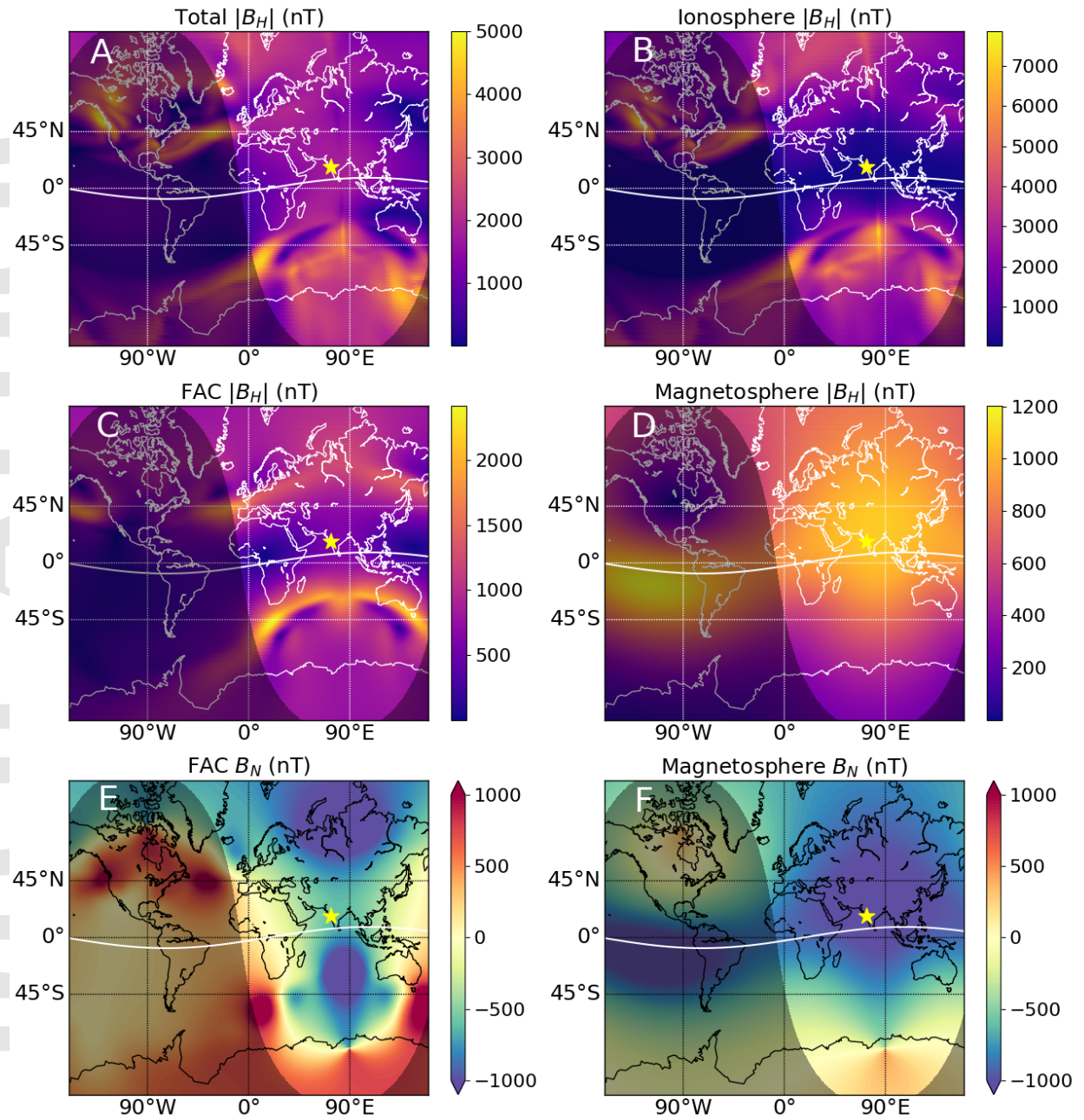
Figure 10. Top row: Comparison between the measured and simulated B_H at Rome (41.9°N, 12.49°E), St. Petersburg (59.93°N, 30.36°E) and Barnaul (53.35°N, 83.78°E) for Simulation 1. Bottom row: breakdown of the B_H contributions for each site. Data for Rome was taken from *Blake et al.* [2020]. Data for St. Petersburg and Barnaul was taken from *Nevanlinna* [2008]. These plots follow Figure 4.

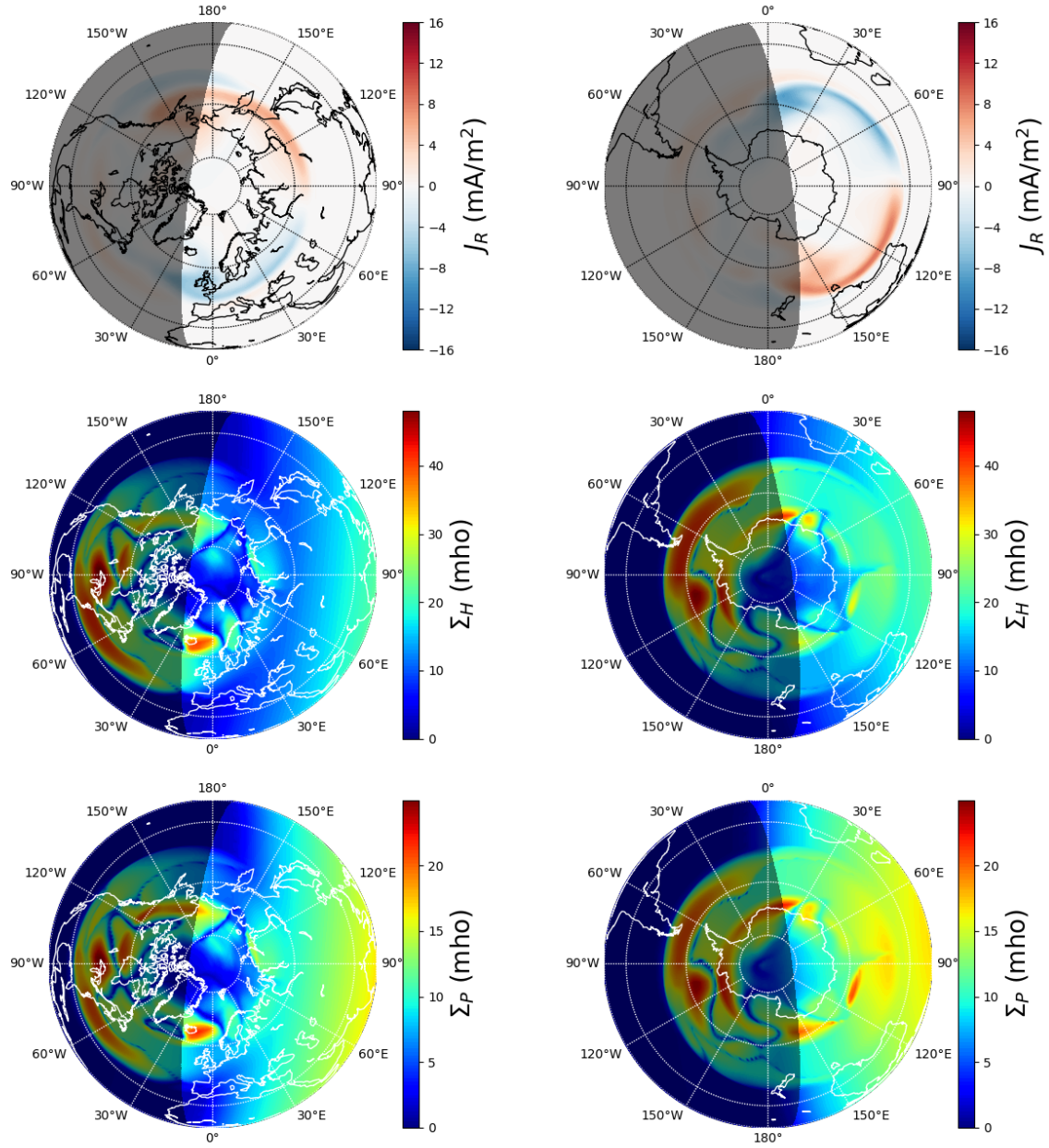


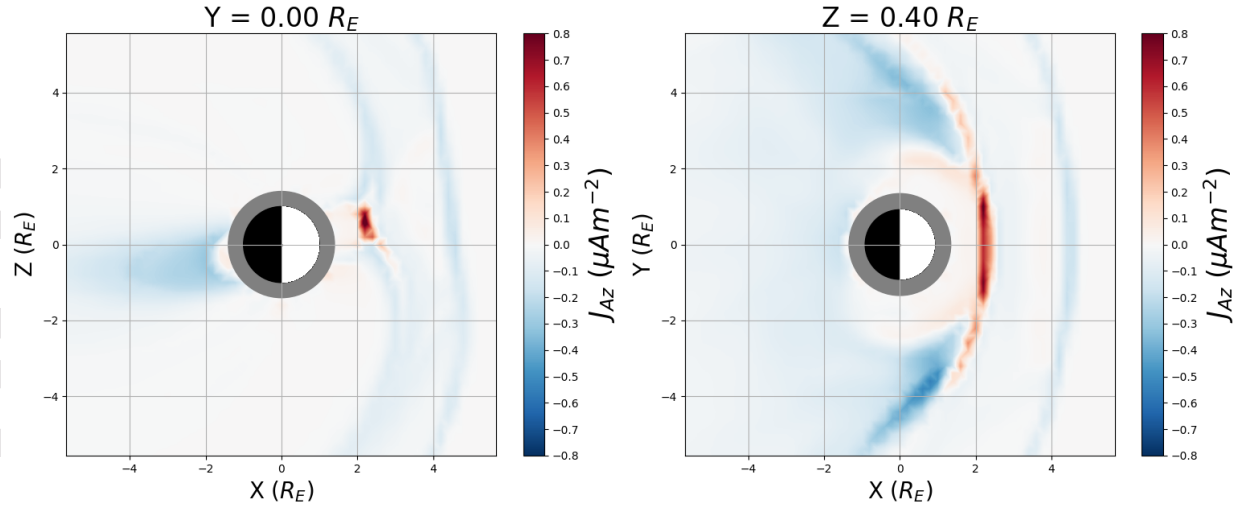


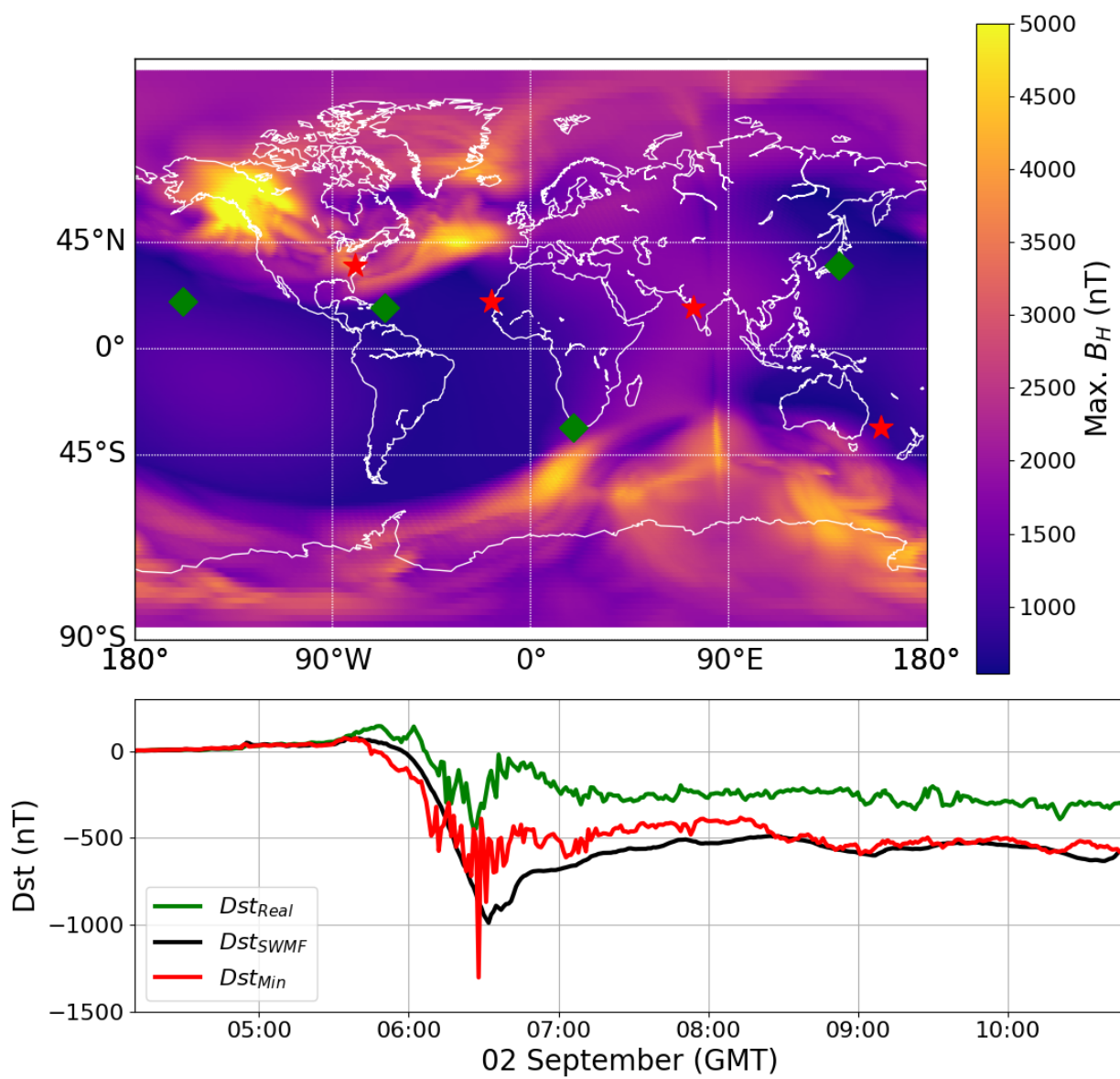


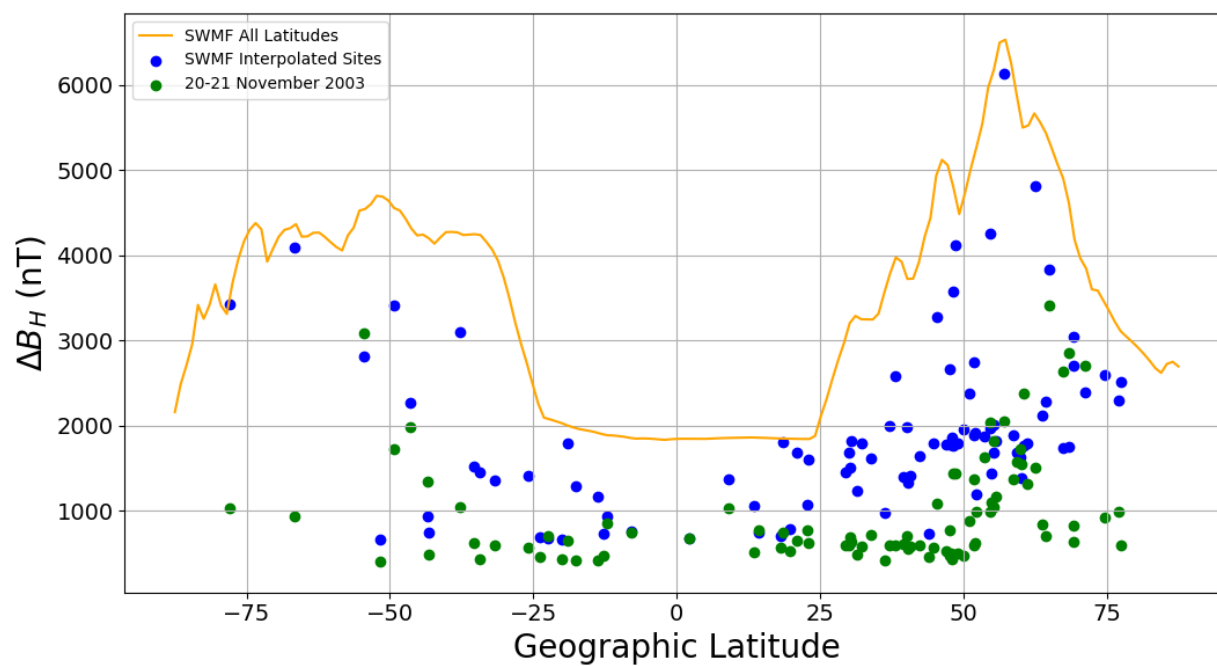


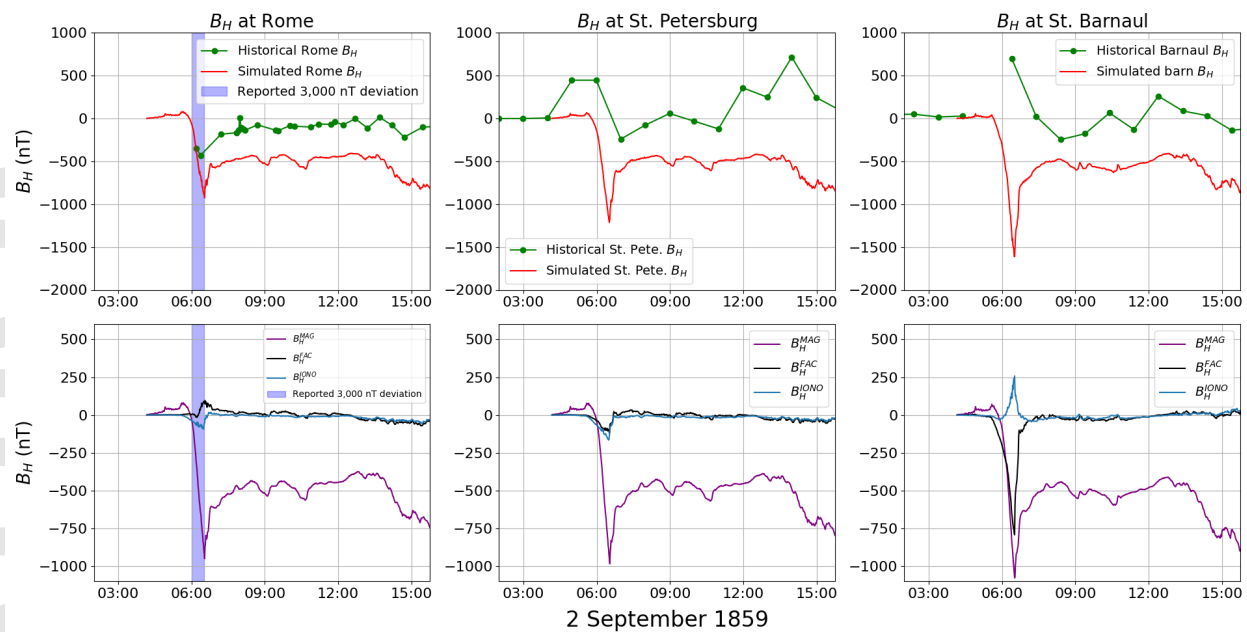


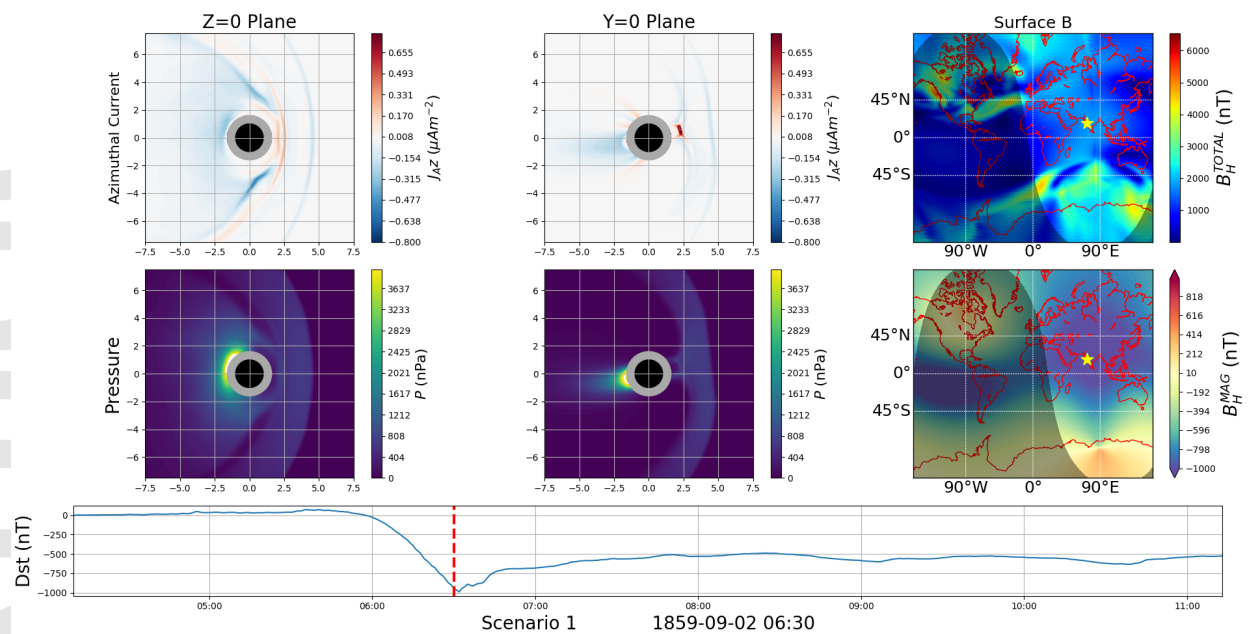












Scenario 3

